



Calhoun: The NPS Institutional Archive
DSpace Repository

Theses and Dissertations

1. Thesis and Dissertation Collection, all items

2000

Design and experimental evaluation of an electro-optical, sigma-delta modulator for wideband digital antennas.

Gillespie, William U.

Monterey, California. Naval Postgraduate School

<http://hdl.handle.net/10945/9246>

This publication is a work of the U.S. Government as defined in Title 17, United States Code, Section 101. Copyright protection is not available for this work in the United States.

Downloaded from NPS Archive: Calhoun



Calhoun is the Naval Postgraduate School's public access digital repository for research materials and institutional publications created by the NPS community. Calhoun is named for Professor of Mathematics Guy K. Calhoun, NPS's first appointed -- and published -- scholarly author.

Dudley Knox Library / Naval Postgraduate School
411 Dyer Road / 1 University Circle
Monterey, California USA 93943

<http://www.nps.edu/library>

NAVAL POSTGRADUATE SCHOOL

Monterey, California



THESIS

**DESIGN AND EXPERIMENTAL EVALUATION OF AN
ELECTRO-OPTICAL, SIGMA-DELTA MODULATOR FOR
WIDEBAND DIGITAL ANTENNAS**

by

William U. Gillespie

December 2000

Thesis Co-Advisors:

Phillip E. Pace
John P. Powers

Approved for public release; distribution is unlimited

REPORT DOCUMENTATION PAGE			Form Approved OMB No. 0704-0188	
Public reporting burden for this collection of information is estimated to average 1 hour per response, including the time for reviewing instruction, searching existing data sources, gathering and maintaining the data needed, and completing and reviewing the collection of information. Send comments regarding this burden estimate or any other aspect of this collection of information, including suggestions for reducing this burden, to Washington headquarters Services, Directorate for Information Operations and Reports, 1215 Jefferson Davis Highway, Suite 1204, Arlington, VA 22202-4302, and to the Office of Management and Budget, Paperwork Reduction Project (0704-0188) Washington DC 20503.				
1. AGENCY USE ONLY (Leave blank)		2. REPORT DATE December 2000	3. REPORT TYPE AND DATES COVERED Master's Thesis	
TITLE AND SUBTITLE : Design and Experimental Evaluation of an Electro-Optical, Sigma-Delta Modulator for Wideband Digital Antennas			5. FUNDING NUMBERS	
6. AUTHOR(S) Gillespie, William U.				
7. PERFORMING ORGANIZATION NAME(S) AND ADDRESS(ES) Naval Postgraduate School Monterey, CA 93943-5000			8. PERFORMING ORGANIZATION REPORT NUMBER	
9. SPONSORING / MONITORING AGENCY NAME(S) AND ADDRESS(ES) Defense Advanced Research Projects Agency, Microsystems Technology Office 3701 North Fairfax Drive, Arlington, VA 22203-1714			10. SPONSORING / MONITORING AGENCY REPORT NUMBER	
11. SUPPLEMENTARY NOTES The views expressed in this thesis are those of the author and do not reflect the official policy or position of the Department of Defense or the U.S. Government.				
12a. DISTRIBUTION / AVAILABILITY STATEMENT Approved for public release; distribution is unlimited.			12b. DISTRIBUTION CODE	
ABSTRACT (maximum 200 words) Electro-optical sigma-delta ($\Sigma\Delta$) analog-to-digital converters (ADCs) use a pulsed laser to oversample an input signal at two Mach-Zehnder interferometer modulators. A fiber lattice accumulator is embedded within a feedback loop around a single-bit quantizer to spectrally shape the quantization noise to fall outside the signal band of interest. Applications of electro-optical $\Sigma\Delta$ ADCs include digitizing wideband radio frequency signals directly at an antenna (digital antenna). The design considerations, construction process and experimental evaluation of the electro-optical $\Sigma\Delta$ ADC are presented. The experimental results are compared with a computer model of the electro-optical $\Sigma\Delta$ sampling and digitization process.				
14. SUBJECT TERMS Sigma-Delta, Optical Sampling, Analog-to-Digital Converters, Optical ADC, Electro-Optical, Digital Antennas, Fiber Lattice, Mach-Zehnder Interferometers			15. NUMBER OF PAGES 110	
			16. PRICE CODE	
17. SECURITY CLASSIFICATION OF REPORT Unclassified	18. SECURITY CLASSIFICATION OF THIS PAGE Unclassified	19. SECURITY CLASSIFICATION OF ABSTRACT Unclassified	20. LIMITATION OF ABSTRACT UL	

THIS PAGE INTENTIONALLY LEFT BLANK

Approved for public release; distribution is unlimited.

**DESIGN AND EXPERIMENTAL EVALUATION OF AN ELECTRO-OPTICAL,
SIGMA-DELTA MODULATOR FOR WIDEBAND DIGITAL ANTENNAS**

William U. Gillespie
Captain, United States Air Force
B.S., University of Notre Dame, 1990


Submitted in partial fulfillment
of the requirements for the degree of

MASTER OF SCIENCE IN ELECTRICAL ENGINEERING

from the

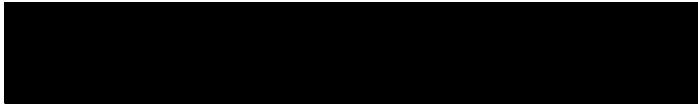
**NAVAL POSTGRADUATE SCHOOL
December 2000**

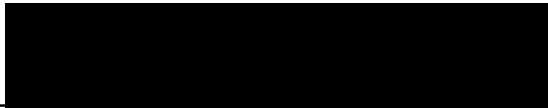
Author:


William U. Gillespie

Approved by:


Phillip E. Pace, Thesis Co-Advisor


John P. Powers, Thesis Co-Advisor


Jeffrey B. Knorr, Chairman
Department of Electrical and Computer Engineering

THIS PAGE INTENTIONALLY LEFT BLANK

ABSTRACT

Electro-optical sigma-delta ($\Sigma\Delta$) analog-to-digital converters (ADCs) use a pulsed laser to oversample an input signal at two Mach-Zehnder interferometer modulators. A fiber lattice accumulator is embedded within a feedback loop around a single-bit quantizer to spectrally shape the quantization noise to fall outside the signal band of interest. Applications of electro-optical $\Sigma\Delta$ ADCs include digitizing wideband radio frequency signals directly at an antenna (digital antenna). The design considerations, construction process and experimental evaluation of the electro-optical $\Sigma\Delta$ ADC are presented. The experimental results are compared with a computer model of the electro-optical $\Sigma\Delta$ sampling and digitization process.

THIS PAGE INTENTIONALLY LEFT BLANK

TABLE OF CONTENTS

I. INTRODUCTION	1
A. BACKGROUND.....	1
B. PRINCIPLE CONTRIBUTIONS.....	2
C. THESIS ORGANIZATION	4
II. ANALOG-TO-DIGITAL SAMPLING TECHNIQUES	7
A. NYQUIST SAMPLING	7
1. Nyquist Theory	7
2. Nyquist Sampling Signal to Noise Ratio.....	8
3. Nyquist Rate Analog-to-Digital Converter Limitations.....	8
B. OVERSAMPLING ANALOG SIGNALS	9
1. Oversampling Theory	9
2. Oversampling Signal to Noise Ratio	11
3. Oversampling Analog-to-Digital Converter Limitations.....	13
C. SIGMA-DELTA ANALOG-TO-DIGITAL CONVERTERS	13
1. Sigma-Delta Analog-to-Digital Converter Operation	14
2. Sigma-Delta Analog-to-Digital Converter Signal to Noise Ratio...	17
3. Second Order Sigma-Delta Analog-to-Digital Architectures	19
D. SUMMARY.....	20
III. CONSTRUCTION OF THE NPS ELECTRO-OPTICAL, SINGLE BIT SIGMA-DELTA MODULATOR	23
A. OVERVIEW OF THE NPS ELECTRO-OPTICAL, SIGMA-DELTA MODULATOR.....	23
B. OPTICAL FIBER.....	26
1. Single Mode Fiber	27
2. Polarization Maintaining Fiber.....	28
C. FIBER SPLICES	29
1. Fusion Splices	30
2. Mechanical Splices	34
D. WAVEFORM SELECTION.....	35
1. Laser Modulation Waveform.....	36
2. RF Antenna Voltage Waveform.....	37
E. SIGNAL OVERSAMPLING PATH DESIGN	38
1. Signal Oversampling Subsystem Operation	38
2. Construction of the Signal Oversampling Subsystem.....	39
F. COMPARATOR CIRCUIT DESIGN	41
G. FIBER LATTICE ACCUMULATOR DESIGN.....	42
H. SUMMARY	45

IV. MEASUREMENTS OF THE NPS ELECTRO-OPTICAL SIGMA-DELTA MODULATOR.....	47
A. OPTICAL POWER LOSS MEASUREMENTS	47
1. Signal Oversampling Subsystem Optical Loss	48
2. Integrated, Optical Sigma-Delta Modulator Optical Loss	49
B. SIGNAL OVERSAMPLING SUBSYSTEM MEASUREMENTS	51
C. COMPARATOR CIRCUIT MEASUREMENTS.....	57
D. PHASE MODULATOR CHARACTERIZATION.....	60
E. SEMICONDUCTOR OPTICAL AMPLIFIER CHARACTERIZATION.....	63
F. FIBER LATTICE ACCUMULATOR MEASUREMENTS.....	66
G. SUMMARY	72
V. CONCLUSIONS AND RECOMMENDATIONS	75
A. LIMITATIONS	75
B. CONCLUSIONS.....	76
C. RECOMMENDATIONS	78
APPENDIX A. COMPONENTS AND EQUIPMENT	81
A. OPTICAL COMPONENTS	81
B. ELECTRICAL EQUIPMENT	82
C. TEST AND OTHER EQUIPMENT	83
APPENDIX B. NPS INTEGRATED, OPTICAL $\Sigma\Delta$ MODULATOR CONNECTIONS AND CONFIGURATION.....	85
APPENDIX C. MATLAB PROGRAMS.....	87
LIST OF REFERENCES	91
INITIAL DISTRIBUTION LIST	93

LIST OF FIGURES

Figure 2.1	Model of a Conventional Analog-to-Digital Converter.	8
Figure 2.2	Quantization Noise Power Spectral Density for Nyquist and Oversampling Rates.	10
Figure 2.3	Block Diagram Representation of an Oversampling ADC Architecture	11
Figure 2.4	Block Diagram of a Typical $\Sigma\Delta$ ADC	15
Figure 2.5	First Order $\Sigma\Delta$ Noise Transfer Function versus the Oversampled Noise Transfer Function	17
Figure 3.1	Block Diagram of the All-Electronic $\Sigma\Delta$ Modulator	23
Figure 3.2	Block Diagram of the NPS Electro-Optical $\Sigma\Delta$ Modulator	24
Figure 3.3	Block Diagram of the Fiber Lattice Accumulator with Feedback Path at Top	25
Figure 3.4	Block Diagram of the Fiber Lattice Accumulator with Feedback Path at Bottom	26
Figure 3.5	Glass Fiber Showing the Inner Core and Outer Cladding	27
Figure 3.6	(a) Polarization Maintaining Fiber Cross Section Compared to (b) Standard Single Mode Fiber	29
Figure 3.7	Splice Loss Distribution for Multimode Fiber	32
Figure 3.8	Splice Loss Distribution for Single Mode Fiber	33
Figure 3.9	(a) Cross Sectional View of an Elastomeric Splice (b) Side View of an Elastomeric Splice	34
Figure 3.10	Splice Loss Distribution for Elastomeric Splices	35
Figure 3.11	Fabry-Perot 1550-nm Laser Drive Signal and Response	37
Figure 3.12	Block Diagram of the Signal Oversampling Subsystem	38
Figure 3.13	Direction Path Comparator Circuit	41
Figure 3.14	Block Diagram of the Fiber Lattice Accumulator	42
Figure 4.1	Magnitude and Direction Path Waveforms from the Signal Oversampling Subsystem	52
Figure 4.2	Oversampled Waveforms in the Direction and Magnitude Paths	53
Figure 4.3	Direction MZI Waveform Exhibiting Folding	54
Figure 4.4	Normalized MZI Transmissivity as a Function of the Applied Voltage for (a) The Magnitude MZI and (b) The Direction MZI	55
Figure 4.5	(a) Voltage Waveforms of the Magnitude and Direction MZIs (b) The Normalized MZI Transmissivity for the Magnitude and Direction MZIs as Determined by Computer Simulation	57
Figure 4.6	Voltage Output of the Direction Comparator Circuit Compared to the Direction Path Waveform	59
Figure 4.7	Block Diagram of the Phase Modulator Characterization Test	62
Figure 4.8	Results of the Phase Modulator Characterization Test	63
Figure 4.9	Block Diagram of the SOA Characterization Test	64
Figure 4.10	Results of the SOA Characterization Test	65

Figure 4.11	Various SOA Operating Points Required for Monotonic Response of the Fiber Lattice Accumulator (a) The Magnitude MZI and (b) The Direction MZI.....	66
Figure 4.12	Fiber Lattice Accumulator Waveform Measurement Locations	67
Figure 4.13	Comparison of (a) the Phase Modulator and (b) Fiber Lattice Accumulator Output Signals	69
Figure 4.14	MATLAB Comparison of the Fiber Lattice Output versus the Phase Modulator Output for (a) Coherent Accumulation and (b) Incoherent Accumulation.....	70
Figure B.1	Layout and Connections for the NPS Electro-Optical $\Sigma\Delta$ Modulator.....	83

LIST OF TABLES

Table 2.1	A Selection of $\Sigma\Delta$ Devices Available from Semiconductor Manufacturers.....	15
Table 3.1	Results of the Laser Drive Waveform Testing.....	36
Table 4.1	Power Budget for the Signal Oversampling Subsystem.....	48
Table 4.2	Power Budget for the Electro-Optical $\Sigma\Delta$ Modulator	50

ACKNOWLEDGEMENT

This thesis would not be complete without recognizing the people that influenced the final product. First and foremost, I would like to thank my advisors, Dr. Phillip Pace and Dr. John Powers for their guidance and patience. Specifically, I am grateful to Professor Pace for the vision and enthusiasm he brought to this Thesis. His greatest contribution is not measured by the development of the project, but in the professional growth of the student. A special thanks to Professor Powers for sparking my interest in optical engineering and for sharing his considerable lab experience with me.

I would also like to thank Mr. Henry Chou for his help and suggestions in the optics lab and Mr. Jeff Knight for his assistance in troubleshooting the comparator circuit. To my family and friends, I thank you for standing by me and for your encouraging words. Finally, I owe a special thanks to my fiancée, Francie. I can't imagine where I would be without your love and understanding. Thank you all.

I. INTRODUCTION

A. BACKGROUND

By converting analog signals into digital signals, information can be processed, analyzed and modified efficiently and accurately using a computer. To achieve the high signal resolutions required for modern communication and signal intercept receivers, sigma-delta ($\Sigma\Delta$) modulation combined with oversampling is often used to digitize the analog signal. Sigma-delta modulators translate the analog signal into a simple digital code (ones and zeros) at a rate much higher than the Nyquist frequency – essentially trading off signal bandwidth for an increase in the signal-to-noise ratio. In addition, sigma-delta modulation provides a method for shaping the quantization noise outside the signal band where it can be removed by digital filtering. High resolution $\Sigma\Delta$ modulators also relax the requirement for precise anti-aliasing filters and amplitude-analyzing components. Sigma-delta techniques combined with the advancements in VLSI technology have allowed engineers to design high performance analog-to-digital converters (ADCs) that provide a high resolution capability for small signal bandwidths.

Sigma-delta ADCs are now commonly found in many low frequency applications such as high fidelity audio, speech processing, metering applications, and voiceband data communications [1]. However, state-of-the-art avionics, wideband spread-spectrum communications, and sensor equipment operate in the microwave region and beyond. These frequencies are outside the speed and resolution capabilities of current CMOS amplitude-analyzing ADC technology [1]. That is, the analog signal must be down-

converted to intermediate frequencies in order to be compatible with the current amplitude-analyzing ADC capabilities. This down-conversion process causes a number of problems including spurious frequencies and intermodulation products. These ADCs are also limited in the resolution that is achievable.

Electro-optics provides a unique way to overcome these problems by coupling the wideband signals into the optical domain thus making the carrier medium a lightwave rather than an electrical current. Additionally, electro-optics provides several advantages over conventional all-electronic circuits. These advantages include increased bandwidth, high-speed switching, low power consumption, insensitivity to vibration, and increased resistance to electromagnetic interference [2]. This thesis examines the construction and experimental testing of an electro-optical $\Sigma\Delta$ modulator designed to operate in the microwave RF bandwidth region.

B. PRINCIPLE CONTRIBUTIONS

One of the first descriptions of an optical implementation of a sigma-delta modulator was by Ying [3]. Later, Atherton and Bewley [4, 5] developed MATLAB Simulink programs to simulate the operational characteristics of an electro-optical $\Sigma\Delta$ modulator. An alternative approach using discrete, multi-quantum well (MQW) modulators was demonstrated in a first-order $\Sigma\Delta$ modulator [6]. This thesis describes the construction and experimental testing of a single bit, electro-optical $\Sigma\Delta$ modulator for use in wideband digital antennas.

The first step in the process of constructing the NPS electro-optical $\Sigma\Delta$ modulator was to examine in detail the MATLAB Simulink operation of the $\Sigma\Delta$ modulator under varying conditions. This step was instrumental in selecting the specific waveforms used to drive the electro-optical $\Sigma\Delta$ modulator. Before actual construction, however, a significant effort was focused on characterizing the fusion splicing capabilities in the Naval Postgraduate School Optical Electronics Laboratory. Through this effort, a shortcoming in the existing fusion splicer was identified and the lab now has a new fusion splicing machine. With a good understanding of the electro-optical approach and of fusion splicing, construction and characterization of individual optical devices started.

Over 30 individual pieces of test equipment and optical components were selected and assembled in the laboratory. The construction and experimentation of the electro-optical $\Sigma\Delta$ modulator was divided into two parts, the signal oversampling subsystem and the fiber lattice accumulator. In constructing the signal oversampling system, a pulsed 1550-nm laser diode source was used to optically sample a RF antenna waveform with an oversampling ratio (OSR) of 12.5. The performance characteristics of this subsystem were compared with the results of the computer simulations from Reference 7. In addition, a comparator circuit for the signal oversampling subsystem was designed and constructed. This circuit completes the sampling system and is used to drive the accumulation in the fiber lattice in the proper direction.

Before beginning construction of the fiber lattice accumulator, the phase modulator and semiconductor optical amplifier (SOA) components were characterized.

The results of the characterization of the phase modulator determined the appropriate output voltage required by the comparator circuit. The characterization test of the SOA, established the correct operating range required for a monotonic linear response of the fiber lattice accumulator.

Finally, a 4-port fiber lattice accumulator was constructed using a phase modulator, a pair of variable ratio directional couplers, a SOA, and a delay loop equal to the inverse of the pulse repetition frequency of the sampling laser ($1/PRF$). The architecture of the fiber lattice accumulator conformed to the $H_{12}(z)$ transfer function as described in Reference 7. The coupling coefficients of the directional couplers were matched with the gain of the SOA to produce a monotonic response of the fiber lattice accumulator.

C. THESIS ORGANIZATION

Chapter II covers the theoretical concepts underlying Nyquist rate analog-to-digital converters and compares the theory with oversampled analog-to-digital converters. The details of sigma-delta modulation are presented and a description of sigma-delta analog-to-digital operation is presented. Finally, a second order sigma-delta modulator is discussed.

Chapter III presents the construction of the NPS electro-optical $\Sigma\Delta$ modulator. The discussion covers the assembly of the signal oversampling subsystem, the direction path comparator circuit, and the fiber lattice structure. The emphasis is on design and

assembly considerations for proper configuration for testing and evaluation of the $\Sigma\Delta$ modulator.

Chapter IV examines the results of the experimental evaluation of the electro-optical $\Sigma\Delta$ modulator. The optical power losses are discussed as well as specific waveform measurements taken from the signal oversampling subsystem and the direction comparator circuit. The results of the phase modulator and semiconductor optical amplifier characterization tests are presented along with their impact on the successful operation of the fiber lattice accumulator. Finally, the results of the testing of the fiber lattice structure are presented.

Chapter V offers conclusions from the construction and evaluation of the electro-optical $\Sigma\Delta$ modulator and lists recommendations for improving the performance of the system.

THIS PAGE INTENTIONALLY LEFT BLANK

II. ANALOG-TO-DIGITAL SAMPLING TECHNIQUES

A. NYQUIST SAMPLING

1. Nyquist Theory

Although real-world signals are analog, there are tremendous advantages when signals are converted into the digital domain. The conversion of analog signals into a digital representation simplifies the transmission, storage and processing of the original analog signal data. Traditional analog-to-digital conversion is described using two separate operations, sampling the signal in time and quantization of the samples in amplitude. Conventional analog-to-digital conversion techniques such as successive approximation, subranging and flash converter circuits sample an analog signal at, or slightly above, the Nyquist rate. Figure 2.1 shows the block diagram of a conventional analog-to-digital converter (ADC) architecture [8]. In this ADC architecture, the input signal $x(t)$ is passed through an anti-aliasing filter to prevent overlap in the signal spectrum. The bandlimited input signal, $\hat{x}(t)$, is then sampled once every T_s seconds creating the amplitude-sampled signal $x(n)$. The sampled values are assigned discrete values by the quantizer resulting in the digital representation of the signal, $y(n)$. Since quantization is a discrete process, quantization noise, $e(n)$, is inherently added to the digital signal at the quantizer. Finally, the digital signal is sent through a low-pass filter to recover the output signal.

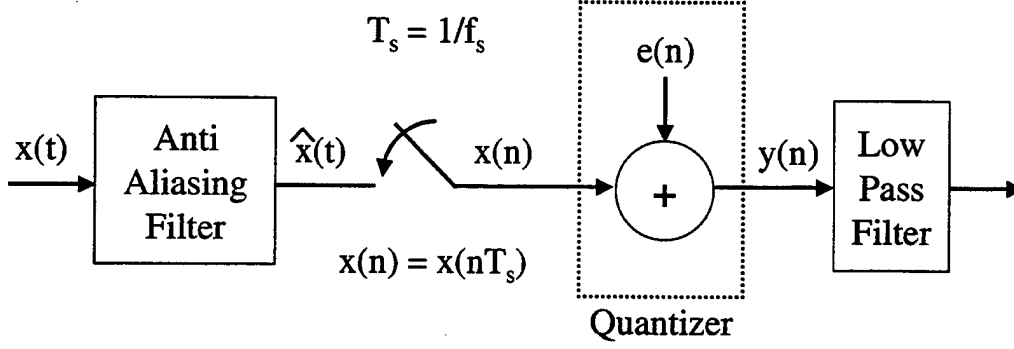


Figure 2.1 Model of a Conventional Analog-to-Digital Converter. From [8].

2. Nyquist Sampling Signal to Noise Ratio

If the quantization error is a uniform (white) noise process then its power (variance) can be expressed as in [8]

$$\sigma_e^2 = \left(\frac{2V}{2^N - 1} \right)^2 / 12 \cong \left(\frac{2V}{2^N} \right)^2 / 12. \quad 2.1$$

If the signal is treated as a zero mean random process with power σ_x^2 , then the signal to quantization noise ratio (SNR) is

$$SNR = 10 \log \left(\frac{\sigma_x^2}{\sigma_e^2} \right) = 10 \log \left(\frac{\sigma_x^2}{V^2} \right) + 4.77 + 6.02N \text{ (dB)}, \quad 2.2$$

where the number of quantization levels is $Q = 2^N$. Note that the SNR will increase by approximately 6 dB for each unit increase in bit resolution, N, for the ADC. [8].

3. Nyquist Rate Analog-to-Digital Converter Limitations

Nyquist rate converters will sample a signal at the full precision or resolution of the converter; however, the resolution of a ADC in VLSI is limited to the technology on which the converter is fabricated. For example an N-bit successive approximation ADC

relies on capacitor components matching to at least one part in 2^N . For a 10-bit ADC, this means the capacitors have to match within $1/1024 \cong 0.1\%$ which is very difficult to do with current VLSI technology [8].

B. OVERSAMPLING ANALOG SIGNALS

1. Oversampling Theory

Oversampling analog-to-digital conversion is a technique that improves upon the resolution available from straight Nyquist rate sampling. As the name implies, samples are acquired from the analog signal at rates much higher than the Nyquist rate. The difference is in the noise introduced by the quantization process. Using oversampling techniques, the quantization noise power, σ_e^2 , is the same as in Nyquist rate sampling, but the frequency distribution of the noise power is different as a result of the higher sampling rate. The oversampling frequency is

$$f_{os} = k \cdot f_{ns} , \quad 2.3$$

where f_{os} is the oversampling frequency, f_{ns} is the Nyquist sampling frequency, and k is the oversampling ratio (OSR) [9]. Since the noise power is uniformly distributed, all the noise power is distributed between $-f_{ns}/2$ to $+f_{ns}/2$ in the case of Nyquist sampling or between $-f_{os}/2$ to $+f_{os}/2$ in the case of oversampling. Figure 2.2 shows the difference in the noise power spectral densities, $P(f)$, between Nyquist sampling and oversampling. Oversampling forces the quantization noise power to be spread over a greater bandwidth. When the signal is finally downsampled and passed through a low-pass filter, the noise power outside the signal band will be attenuated.

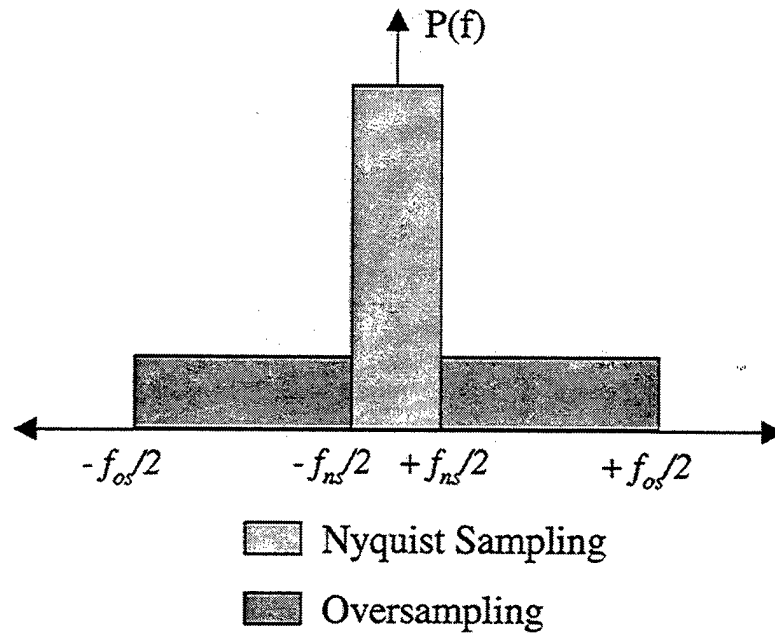


Figure 2.2 Quantization Noise Power Spectral Density for Nyquist and Oversampling Rates. From [8].

Figure 2.3 shows a block diagram of an oversampling ADC architecture. In this architecture, the input signal, $x(t)$, is again sent through an anti-aliasing filter to prevent overlap in the signal spectrum. The input signal amplitude is sampled at the oversampling frequency, f_{os} , creating the sampled input signal, $x(n)$. The sampled input signals are assigned discrete values by the quantizer resulting in the digital representation of the signal, $y(n)$. However, the quantization noise, $e(n)$, is spread over the oversampling frequency spectrum and much of it can be removed by the low-pass filter. Finally, to completely recover the signal, the output samples, $y(n)$, must then be down-sampled to the Nyquist frequency.

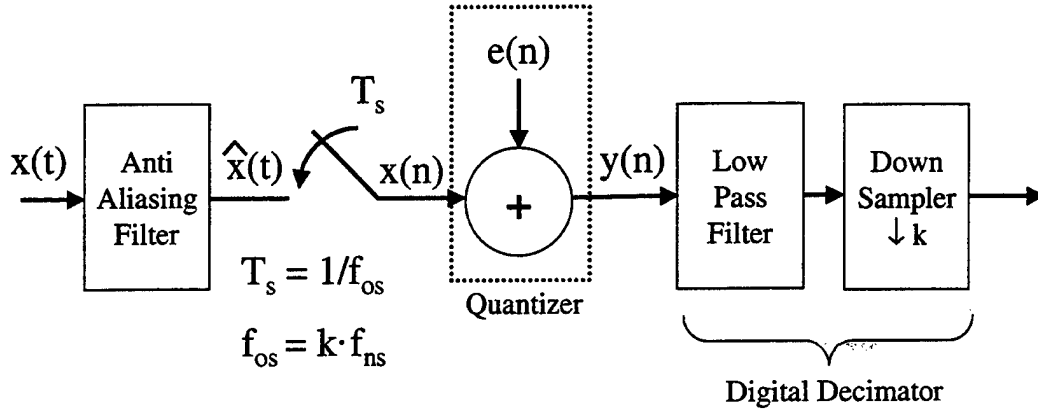


Figure 2.3 Block Diagram Representation of an Oversampling ADC Architecture. From [8].

2. Oversampling Signal to Noise Ratio

From the block diagram in Figure 2.3 , the output can be written in the Z domain

as

$$Y(z) = X(z)H_x(z) + E(z)H_e(z), \quad 2.4$$

where $H_x(z)$ and $H_e(z)$ are the signal transfer function and noise transfer function, respectively, and $Y(z)$, $X(z)$, and $E(z)$ are the Z transforms of the output signal, input signal and the quantization error process. If $X(z)$ and $E(z)$ are stationary random processes, then their respective power spectral densities at the output of the converter are related to their input power spectral densities by

$$P_{xy}(f) = P_x(f)|H_x(f)|^2 \quad 2.5$$

and

$$P_{ey}(f) = P_e(f)|H_e(f)|^2. \quad 2.6$$

For the oversampled case, $|H_x(f)|^2$ and $|H_e(f)|^2$ are equal to one. The quantization noise is assumed to be white such that $P_e(f) = \sigma_e^2/f_{os}$ and therefore $P_{ey}(f) = \sigma_e^2/f_{os}$. If an ideal low-pass filter with cutoff frequency, f_c , is used at the output of the converter, the in-band noise power, σ_{ey}^2 , can be expressed as

$$\sigma_{ey}^2 = \int_{-f_c}^{+f_c} P_{ey}(f) df = \int_0^{+f_c} 2 \left(\frac{\sigma_e^2}{f_{os}} \right) df = \sigma_e^2 \left(\frac{2f_c}{f_{os}} \right). \quad 2.7$$

Note that $2f_c = f_{ns}$ (Nyquist frequency) and that the in-band noise power is actually reduced by the inverse of the oversampling ratio (OSR),

$$\sigma_{ey}^2 = \sigma_e^2 \left(\frac{f_{ns}}{f_{os}} \right) = \sigma_e^2 \left(\frac{f_{ns}}{k \cdot f_{ns}} \right) = \sigma_e^2 \left(\frac{1}{OSR} \right). \quad 2.8$$

Therefore the signal-to-noise ratio for an oversampling ADC can be written as

$$SNR = 10 \log \left(\frac{\sigma_x^2}{\sigma_{ey}^2} \right) = 10 \log \left(\frac{\sigma_x^2 \cdot OSR}{\sigma_e^2} \right) = 10 \log \left(\frac{\sigma_x^2}{\sigma_e^2} \right) + 10 \log(OSR) \quad (dB). \quad 2.9$$

If the oversampling ratio is represented as $OSR = 2^r$, the signal-to-noise ratio becomes

$$SNR = 10 \log \left(\frac{\sigma_x^2}{\sigma_e^2} \right) + 10 \log(2^r) = 10 \log \left(\frac{\sigma_x^2}{\sigma_e^2} \right) + 3.01r \quad (dB) \quad 2.10$$

where every unit increment in r represents a doubling of the sampling ratio. From this equation, we see that every time the oversampling ratio is doubled (or r is incremented by

one), the signal-to-noise ratio improves by approximately 3 dB. In other words, the resolution of the ADC improves by one-half bit. [10].

3. Oversampling Analog-to-Digital Converter Limitations

The oversampling analog-to-digital architecture is ultimately a trade off of speed versus resolution. The higher bit-resolution (higher signal-to-quantization noise ratio) is obtained by operating the sampling and quantization circuits at much higher speeds than a comparable Nyquist rate ADC. In many cases, the speed of the VLSI technology presents an upper limit on the bandwidth of the analog signals that can be oversampled. For high resolution analog-to-digital conversion, $f_{os} \gg f_{ns}$ but f_{os} must not exceed the maximum circuit speed available. For example, consider a sinusoid with amplitude 1 volt and a signal power of $V^2/2 = 0.5$ watts applied as the input to a oversampled ADC with a 128 kHz signal band. If the desired resolution is 16 bits, a SNR of 98 dB will be required. If we use an 8-bit ADC ($N = 8$) in an oversampled architecture, the required oversampling frequency can be calculated as $f_{os} = 16.4$ GHz [8]. Because electronic circuits are limited in their frequency response, we can see this in turn limits the resolution that can be gained by oversampling higher frequency analog signals.

C. SIGMA-DELTA ANALOG-TO-DIGITAL CONVERTERS

In the discussion of the oversampling ADC, the output signal was represented in the Z domain as

$$Y(z) = X(z)H_x(z) + E(z)H_e(z). \quad 2.11$$

For oversampling architectures, the signal transfer function, $H_x(z)$, and the noise transfer function, $H_e(z)$, were both unity. However, the noise transfer function can be modified from unity to shape the quantization noise out of the signal band and leave the signal of interest undisturbed. This is sometimes termed ‘noise-shaping’ and is the centerpiece behind the sigma-delta ($\Sigma\Delta$) modulation technique. The power of $\Sigma\Delta$ modulation is it allows the use of low bit-resolution internal ADCs (resolutions as low as $N = 1$) to achieve a much higher bit-resolution overall for the ADC. Several examples of $\Sigma\Delta$ analog-to-digital, digital-to-analog, and digital signal processing processors manufactured on chip codecs are shown in Table 2.1 [11]. The table shows the upper frequency that the device can accept as input, the anticipated bit-resolution of the device and the oversampling ratio used. To obtain the maximum oversampling frequency, multiply the input frequency by the oversampling ratio.

1. Sigma-Delta Analog-to-Digital Converter Operation

A typical first-order $\Sigma\Delta$ ADC block diagram is shown in Figure 2.4. The difference between a $\Sigma\Delta$ ADC and the amplitude-analyzing ADCs discussed previously is that the quantized signal is not the sampled signal $x(n)$, but rather it is the difference between the sampled input and a filtered version of the quantized output, $y(n)$. The filter is called the feed-forward loop filter and it is a discrete time integrator with a transfer function of $z^{-1}/(1-z^{-1})$.

DEVICE	INPUT FREQUENCY	RESOLUTION (bits)	OVERSAMPLING RATIO
Burr Brown PCM 1710	48 kHz	20	384
Motorola DSP56ADC16	100 kHz	16	64
Burr Brown PCM 1760	48 kHz	20	64
Texas Instruments TLC320AD58C	48 kHz	18	64
National Semiconductor ADC16071	48 kHz	16	64
Nippon SM5872A/B	44.1 kHz	16	384
Crystal Semiconductor CS4215	48 kHz	16	64
Crystal Semiconductor CS4328	48 kHz	18	64
Crystal Semiconductor CS5390	48 kHz	20	64
Analog Devices AD776	100 kHz	16	64
Analog Devices AD1879	48 kHz	18	64
Analog Devices AD28msp02	8 kHz	16	128
Philips SAA7360GP	48 kHz	18	128
Philips SAA7350(A)	48 kHz	20	128

Table 2.1 A Selection of $\Sigma\Delta$ Devices Available from Semiconductor Manufacturers. From [11].

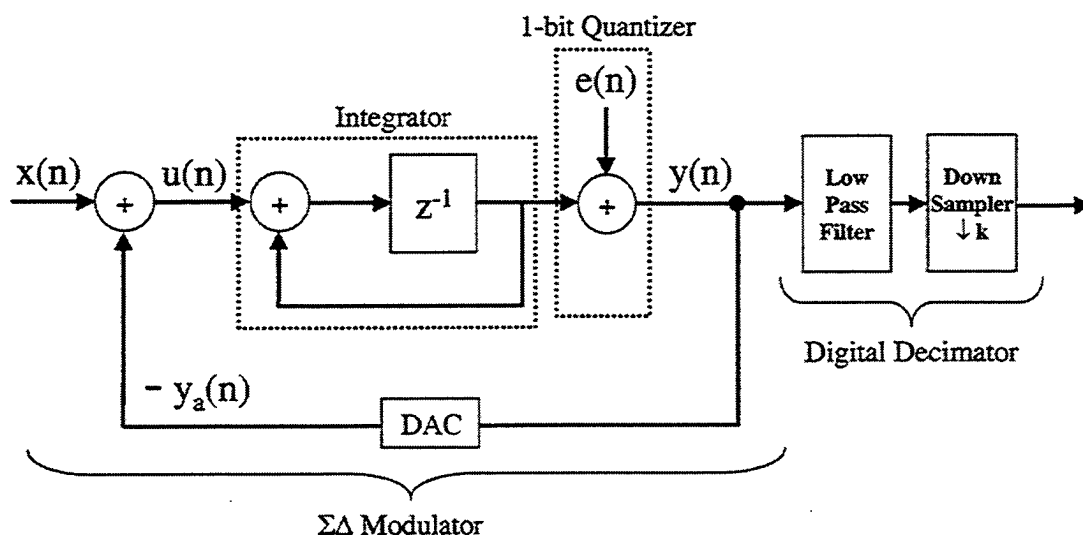


Figure 2.4 Block Diagram of a Typical $\Sigma\Delta$ ADC. From [10].

Therefore, the Z transform of the output can be rewritten as

$$Y(z) = X(z)z^{-1} + E(z)(1 - z^{-1}). \quad 2.12$$

The time domain output is represented as the sum of the previous sampled input and the difference between the n^{th} and $n^{\text{th}}-1$ samples of the quantization noise, or

$$y(n) = x(n-1) + [e(n) - e(n-1)]. \quad 2.13$$

It is important to note the presence of the digital-to-analog converter (DAC) in the system block diagram. The linearity of this device is very important to the operation of the $\Sigma\Delta$ analog-to-digital modulator, since any non-linearities in the DAC will be added as noise to the input signal, $x(n)$. This noise will be reduced if oversampling is performed but it is not affected by the noise-shaping of the $\Sigma\Delta$ architecture. Therefore, it is desirable to use a single-bit DAC with a corresponding single-bit quantizer since this combination is linear in response [10].

As Figure 2.5 shows, the first-order noise transfer function attenuates the low frequency noise compared to the relative amplification at higher frequencies. However, the amplified high frequency noise is outside the signal band and is removed with the low-pass filter.

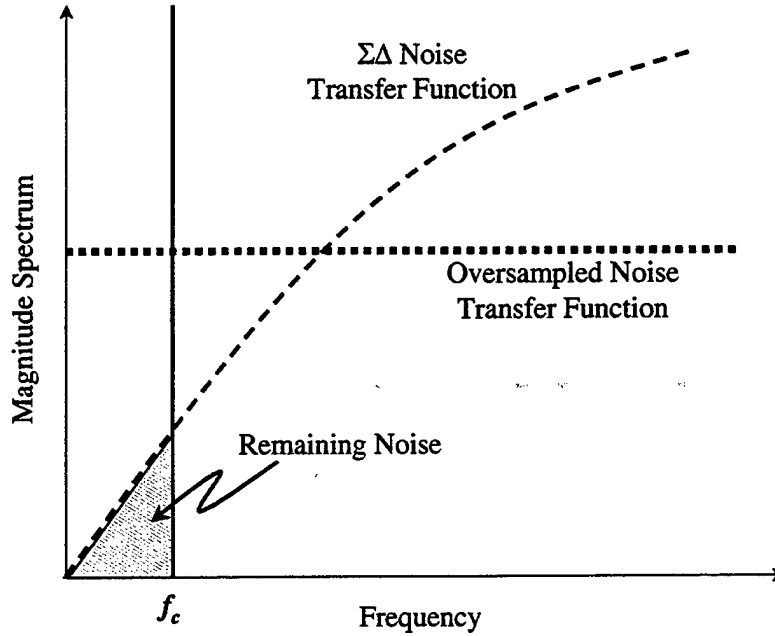


Figure 2.5 First Order $\Sigma\Delta$ Noise Transfer Function versus the Oversampled Noise Transfer Function. From [8].

2. Sigma-Delta Analog-to-Digital Converter Signal-to-Noise Ratio

Using the same method as outlined in the oversampling ADC discussion and the fact that $H_x = z^{-1}$ and $H_e = (1 - z^{-1})$ we can calculate the in-band noise power as

$$\sigma_{ey}^2 = \int_{-f_c}^{+f_c} P_{ey}(f) df = \sigma_e^2 \cdot \frac{\pi^2}{3} \left(\frac{2f_c}{f_{os}} \right)^3. \quad 2.14$$

The signal-to-noise ratio in dB is

$$SNR = 10 \log \left(\frac{\sigma_x^2}{\sigma_{ey}^2} \right) = 10 \log(\sigma_x^2) - 10 \log(\sigma_e^2) - 10 \log \left(\frac{\pi^2}{3} \right) + 30 \log \left(\frac{f_{os}}{f_{ns}} \right) \quad (dB). \quad 2.15$$

If the oversampling ratio, $f_{os}/f_{ns} = OSR$, is replaced with 2^r , the SNR becomes

$$SNR = 10 \log(\sigma_x^2) - 10 \log(\sigma_e^2) - 5.17 + 9.03r \quad (dB). \quad 2.16$$

Therefore, every time the oversampling ratio (OSR) is doubled (or, equivalently, for every unit increment in r), the signal-to-noise ratio will improve by approximately 9 dB. This translates to an extra 1.5 bits of resolution for every doubling of the oversampling ratio in the $\Sigma\Delta$ ADC.

Reexamine the problem in the oversampling discussion of a sinusoid with amplitude 1 volt and a signal power of $V^2/2 = 0.5$ watts. Using only an oversampling architecture, the required oversampling frequency was $f_{os} = 16.4$ GHz. If the same signal is applied as the input to an oversampled $\Sigma\Delta$ ADC with a 128 kHz signal band and the desired resolution is 16 bits, a SNR of 98 dB will still be required. However, if we use an 8-bit ADC ($N = 8$) in this oversampled $\Sigma\Delta$ architecture, the new required oversampling frequency is calculated as $f_{os} = 618.4$ MHz. Compared to the f_{os} calculated when oversampling was the only analog-to-digital technique employed, the $\Sigma\Delta$ modulation technique provides a significant reduction in the oversampling frequency. Therefore, sigma-delta modulation places the oversampling frequency within range of current sampling frequencies.

3. Second-Order Sigma-Delta Analog-to-Digital Architectures

The basic building blocks for the $\Sigma\Delta$ analog-to-digital modulator, a discrete time integrator, a single bit quantizer, and a digital-to-analog converter can be extended to create more complex systems. The design of these analog-to-digital architectures presents tradeoffs of circuit complexity, operating stability, resolution and speed. In a second-order $\Sigma\Delta$ modulation scheme, two discrete time integrators are linked together and the noise transfer function becomes $z^{-1}/(1-z^{-1})^2$ creating a Z domain output of

$$Y(z) = X(z)z^{-1} + E(z)(1 - z^{-1})^2. \quad 2.17$$

Assuming low-pass filtering at the output and a white noise model, the analysis of the in-band noise yields the following signal-to-noise ratio

$$SNR = 10 \log \left(\frac{\sigma_x^2}{\sigma_{ey}^2} \right) = 10 \log(\sigma_x^2) - 10 \log(\sigma_e^2) - 10 \log \left(\frac{\pi^4}{5} \right) + 50 \log \left(\frac{f_{os}}{f_{ns}} \right) \quad (dB). \quad 2.18$$

Again letting $f_{os}/f_{ns} = OSR = 2^r$, the SNR becomes

$$SNR = 10 \log(\sigma_x^2) - 10 \log(\sigma_e^2) - 12.90 + 15.05r \quad (dB). \quad 2.19$$

Thus for every unit increase in r , or doubling of the oversampling ratio, the signal-to-noise ratio will improve by approximately 15 dB and the resolution will improve by 2.5 bits. In a similar manner the $\Sigma\Delta$ topology can be linked together to create higher order converters. In each case, the SNR will increase by approximately 6 dB and the bit resolution will improve by one bit from the previous order architecture. However, it is difficult to characterize the gain of the one-bit quantizer because it depends upon the quantizer input, i.e., the smaller the input, the larger the gain. Additionally, limit cycle oscillations within the modulator can cause instability in the amplitude saturating the integrator outputs. For this reason, higher order $\Sigma\Delta$ architectures require more precise circuitry and have not found much use outside the laboratory environment. [8].

D. SUMMARY

There are two techniques important to the operation of state-of-the-art ADCs, oversampling of the analog signal and $\Sigma\Delta$ modulation. The first technique, oversampling, is important because it spreads the quantization noise over a wider frequency band thus reducing the in-band quantization noise. This results in a 3 dB increase of the SNR or an improvement of one-half bit in resolution every time the oversampling ratio (OSR) is doubled. The second technique, $\Sigma\Delta$ modulation, has the added benefit of shaping the quantization noise such that a majority of the remaining in-band quantization noise is greatly attenuated. Using first-order $\Sigma\Delta$ modulation, the SNR can be improved by 9 dB equating to an increase in the bit resolution by 1.5 bits. However, all-electronic,

oversampled $\Sigma\Delta$ architectures are ultimately limited to lower RF frequencies because of the relatively slower CMOS speeds compared to pulsed mode-locked laser frequencies.

A possible solution is an electro-optical approach that can couple higher bandwidth RF signals into the optical domain where light pulses from a mode-locked laser can oversample the RF signal. This is the basis behind the design of the NPS electro-optical $\Sigma\Delta$ modulator.

THIS PAGE INTENTIONALLY LEFT BLANK

III. CONSTRUCTION OF THE NPS ELECTRO-OPTICAL, SINGLE-BIT SIGMA-DELTA MODULATOR

The NPS electro-optical sigma-delta ($\Sigma\Delta$) modulator is a first-order architecture and uses the oversampling and noise shaping techniques described in Chapter II. The modulator can be broken down into two primary subsystems, the optical oversampling subsystem and the fiber lattice subsystem. Figure 3.2 details the overall design of the electro-optical $\Sigma\Delta$ modulator and will be referred to throughout the chapter.

A. OVERVIEW OF THE NPS ELECTRO-OPTICAL, SIGMA-DELTA MODULATOR

Many similarities exist between the all-electronic $\Sigma\Delta$ modulator architecture shown in Figure 3.1 and the block diagram of the NPS electro-optical $\Sigma\Delta$ modulator shown in Figure 3.2 [7]. Just as the all-electronic $\Sigma\Delta$ modulator requires an oversampling component, an integrator, and a single-bit quantizer, the electro-optical antenna has equivalent sampling, accumulation and quantization devices. In the electro-optical

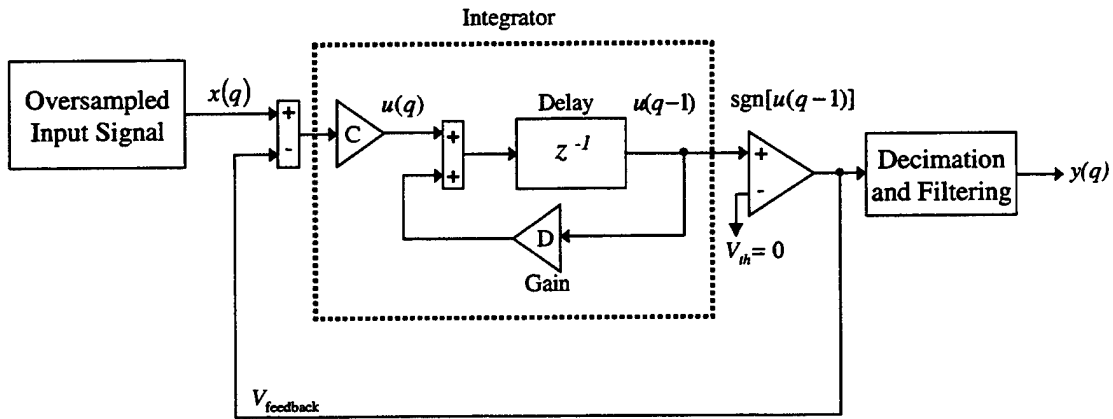


Figure 3.1 Block Diagram of the All-Electronic $\Sigma\Delta$ Modulator. From [7].

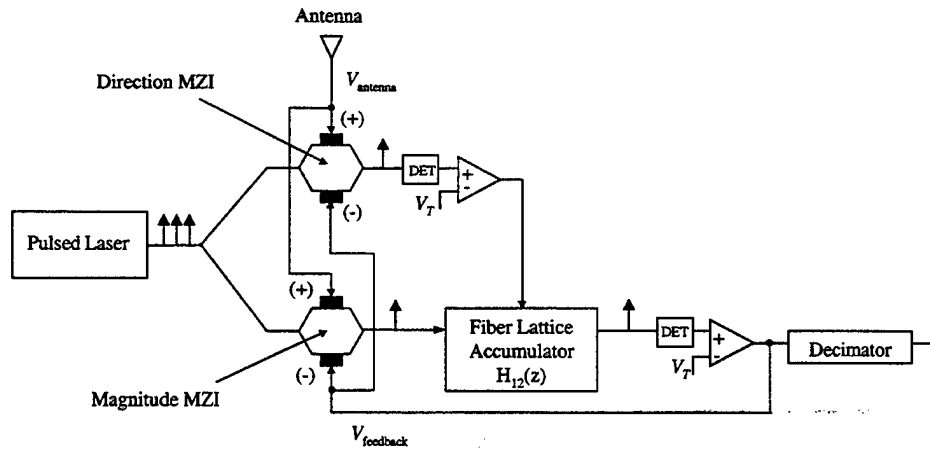


Figure 3.2 Block Diagram of the NPS Electro-Optical $\Sigma\Delta$ Modulator. From [7].

$\Sigma\Delta$ modulator, the sampling is performed by a high pulse-repetition-frequency (PRF) diode laser and two Mach-Zehnder interferometer (MZI) modulators. The analog RF signal is coupled directly to one of the electrodes in each of the MZIs. Since light intensity can only take on positive values, the RF signal is connected to the MZIs – one to represent magnitude, or signal amplitude information and the other for direction, or polarity information.

To be accomplish this, the transmissivities of the MZIs are biased $\pi/2$ radians out of phase with respect to each other. In this way, ambiguity in the magnitude path intensity can be resolved by determining the corresponding direction-path intensity. The light intensity value in the direction path is converted to a voltage by the photodetector and evaluated by a comparator circuit. If the voltage exceeds the comparator circuit threshold, the comparator outputs 0 volts to the phase modulator. The light intensity from the magnitude path will then pass through the phase modulator and into the fiber lattice accumulator in-phase. If the voltage is below the designed threshold, a voltage of V_π is output by the comparator circuit and delivered to the phase modulator. When this occurs,

the light from the magnitude path will pass into the fiber lattice accumulator with a π radians phase shift. Therefore, it is at the phase modulator where the direction information and magnitude information are recombined.

The fiber lattice accumulator shown in Figure 3.3 is the equivalent of the discrete-time integrator of the all-electronic $\Sigma\Delta$ ADC and is where the laser pulses from the signal oversampling subsystem and the phase modulator are accumulated. A more conventional configuration of the fiber lattice, with the feedback path on the bottom of the figure, is shown in Figure 3.4. A light pulse from the phase modulator is transferred to the first of

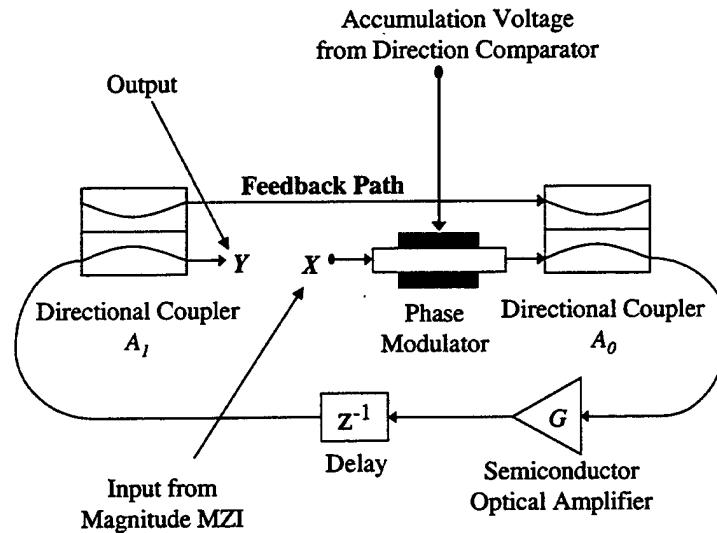


Figure 3.3 Block Diagram of the Fiber Lattice Accumulator with Feedback Path at Top. From [9].

two variable ratio couplers, A_0 , where it combines constructively or destructively with the previous light pulse. The resulting light pulse is then amplified by a semiconductor optical amplifier in the feed forward path and sent to the second variable ratio coupler, A_1 . At this second coupler the light power is divided again. Part of the light power is transferred to the output of the fiber lattice, Y . The remaining portion of the light energy

is fed back to A_0 where it recombines constructively or destructively with the next light pulse from the phase modulator. In Reference 5, Atherton develops reference tables for

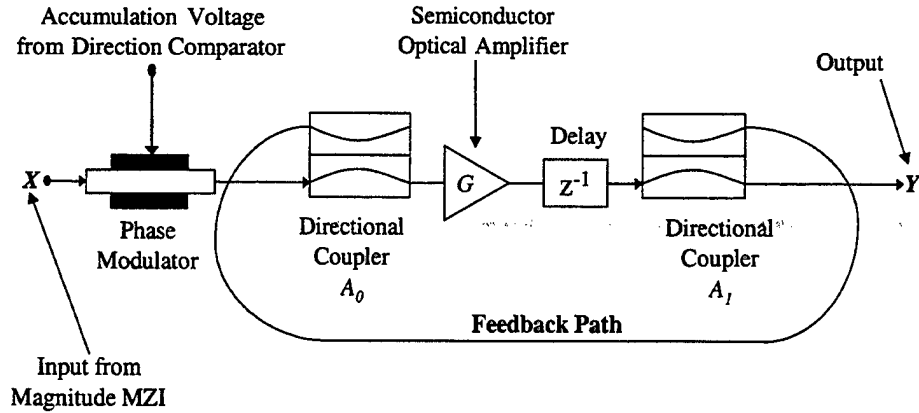


Figure 3.4 Block Diagram of the Fiber Lattice Accumulator with Feedback Path at Bottom. After [10].

matching the A_0 and A_1 coupling coefficients to the semiconductor optical amplifier gain, G , in order to obtain a linear response from the fiber lattice accumulator. Finally, the light power output by the fiber lattice is transferred to a photodetector and comparator circuit.

B. OPTICAL FIBER

The electro-optical $\Sigma\Delta$ modulator is constructed using two types of optical fiber, single-mode (SM) fiber and polarization maintaining (PM) fiber. Combined, the total amount of optical fiber used in the construction of the $\Sigma\Delta$ modulator is approximately 1034.7 meters. Single-mode fiber is primarily used throughout the design of the modulator; however, polarization maintaining fiber is used prior to several of the integrated optical components to enhance coherent light transmission.

1. Single Mode Fiber

In general, optical fiber is comprised of an inner, glass core which provides the waveguide path for the light. It is surrounded by an outer cladding as shown in Figure 3.5. The index of refraction in the core, n_1 , is slightly higher than that in the cladding. Light that strikes the boundary between the core and cladding is confined to the core by total internal reflection thus producing the waveguide for the light [12]. The core diameter of single-mode fiber is usually less than $10\text{ }\mu\text{m}$ and the cladding diameter is usually at least $125\text{ }\mu\text{m}$ across for handling reasons. Additionally, most optical fibers have an acrylic coating and plastic sheathing for protection [13]. If a fiber does not have the plastic sheathing, it is called 'bare fiber'. The majority of the fiber in the electro-optical $\Sigma\Delta$ modulator is bare fiber with the exception of specific component input and output fibers which are cabled for handling stresses.

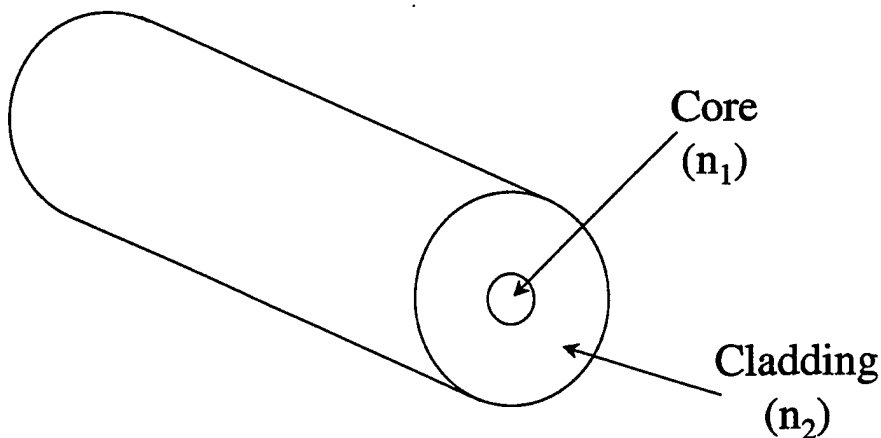


Figure 3.5 Glass Fiber Showing the Inner Core and Outer Cladding. From [12].

Single-mode fiber is designed to allow only one guided mode, the fundamental mode, to travel down the core of the fiber. Because the core radius is only several times

the light wavelength, single-mode fiber prevents higher order modes from existing. This promotes light to propagate directly down the center of the core instead of continually reflecting off the core-cladding boundary. The region physically occupied by light in a single-mode fiber is called the mode field diameter and refers to the optical power distribution of the wave within a single-mode fiber. [12].

2. Polarization Maintaining Fiber

Laser light is an electromagnetic wave with an associated electric and magnetic field. The electric and magnetic fields are normal to each other and propagate in a direction perpendicular to both fields. Standard single-mode fiber is insensitive to polarization and will carry light in both horizontal and vertical polarization modes. However as light propagates in the fiber, mechanical stresses and environmental changes can randomly rotate this polarization. For active modulation to occur, some integrated optical devices require the polarization remain unchanged as it travels through the fiber.

Polarization maintaining (PM) fiber is designed to isolate the two orthogonal polarizations from each other by effectively creating two propagation paths within the fiber core. This is accomplished by adding two stress-induced birefringent fibers which apply asymmetric stresses to the core of the fiber as shown in Figure 3.6. The plane in-line with the stress members is referred to as the slow axis. The plane perpendicular to the slow axis defines the fast axis. When linearly polarized light from a laser is guided into either the fast or slow axis, the light will remain on that axis and keep its polarization state.

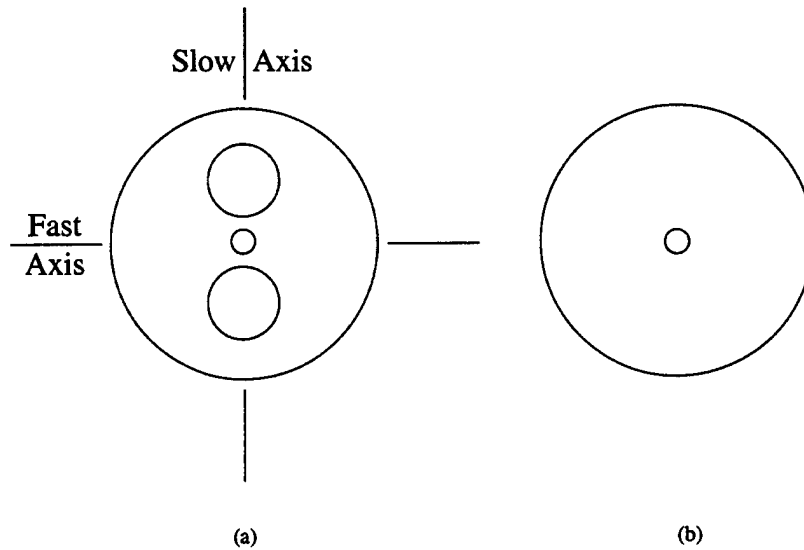


Figure 3.6 (a) Polarization Maintaining Fiber Cross-Section Compared to (b) Standard Single-Mode Fiber. From [13].

The NPS electro-optical $\Sigma\Delta$ modulator uses Fujikura brand UV-400 Panda PM fiber as the input to the Mach-Zehnder interferometers and as the input and output fibers of the phase modulator. The mode field diameter of the Fujikura PM fiber is $10.5\text{ }\mu\text{m}$ and the fiber has a maximum attenuation factor of 0.5 dB/km [14]. For the electro-optical $\Sigma\Delta$ modulator, approximately 3.9 meters of PM fiber are used in the signal oversampling subsystem and 3.3 meters are used in the fiber lattice.

C. FIBER SPLICES

The fibers in the $\Sigma\Delta$ modulator were spliced together using two types of splices, fusion and mechanical splices. Fusion splices are permanent and were used to fix a component or fiber into place. Mechanical splices are temporary and were used in the testing and characterization of optical components prior to permanently including them in

the construction of the $\Sigma\Delta$ modulator. For both fusion and mechanical splices, the estimated optical power loss at the junction of the splice is a critical parameter. An effort was made to characterize the splice loss for both fusion and mechanical splices. This was viewed as necessary since splice losses created in the construction of the electro-optical $\Sigma\Delta$ modulator could not be easily or accurately measured. However, before construction of the $\Sigma\Delta$ modulator began, the Sumitomo 11X fusion splicer experienced a motor failure in its alignment mechanism. It was eventually replaced in the lab by a Sumitomo Type 36 and Sumitomo Type 35SE-RC fusion splicer. Both of these fusion splicers provide an estimation of the splice loss. Therefore, the multimode and single-mode splice loss distributions provided in subsection C.1 are for completeness only and do not reflect the splice losses experienced during construction.

1. Fusion Splices

Fusion splices are permanent glass welds that physically bonds two fiber strands together creating a continuous waveguide. First the fiber ends are stripped of the protective plastic and acrylic coating that surrounds the core-cladding. The glass is then scored and broken using a manual cleaving device. This produces a 90 degree cut to the face of the fiber ends. The bare fiber is cleaned using ethyl alcohol and cotton swabs to remove contaminants. However, special care must be taken not to rub the glass too vigorously which can create a static charge that attracts dust particles. The fibers are placed in the V-grooves of a fusion splicing machine which provide a coarse alignment of the fiber ends. Using a microscope, the fiber ends are maneuvered such that an approximate 10- μm gap separates them. A laser source is then connected to the free end

of one fiber and an optical multimeter to the end of the other fiber. The horizontal and vertical axes can then be manually aligned such that maximum power is received at the multimeter. A brief electrical arc is applied across the gap fusing the two fiber ends together creating a continuous waveguide.

One of the major advantages of using fusion splices is the low attenuation across the junction of the finished splice. Typical losses from a fusion splice are between 0.1 dB and 0.2 dB [15]. This attenuation is the result of two different loss mechanisms, intrinsic and extrinsic losses. Intrinsic losses are caused by the physical differences between the two fibers. These differences include variations in the core diameters, the ellipticity of the cores, and the index profiles of the fibers. Extrinsic losses are caused by the nature of the splice itself. Lateral misalignment, angular misalignment, cleave quality, and fiber end contamination all contribute to extrinsic losses. However extrinsic losses can be minimized by strict control of the splicing procedures. [12].

One of the significant differences between the fusion splicing process described above and the fusion splicing process used in the construction of the electro-optical $\Sigma\Delta$ modulator was that optical power measurements could not be used to align the fiber ends. The fiber used in the electro-optical $\Sigma\Delta$ modulator contains optical devices such as the 3-dB coupler, the Mach-Zehnder interferometers, and the phase modulator inserted between the fiber ends. These devices preclude using the maximum optical power method for determining proper alignment of the fiber ends because they intercept the light from the

optical source. Therefore, splice losses obtained using the Sumitomo 11X Splicer were measured to determine the mean splice loss for multimode and single-mode fiber.

Figure 3.7 shows the splice loss distribution for 25 fusion splices using multimode fiber. Multimode fiber has a larger core diameter and therefore is not as sensitive to core misalignments or imperfections in the fusion splice. The core diameter for the multimode fiber used in this series was 62.5 μm . The results show a mean splice loss of 0.15 dB which is within the range of experimental results [15].

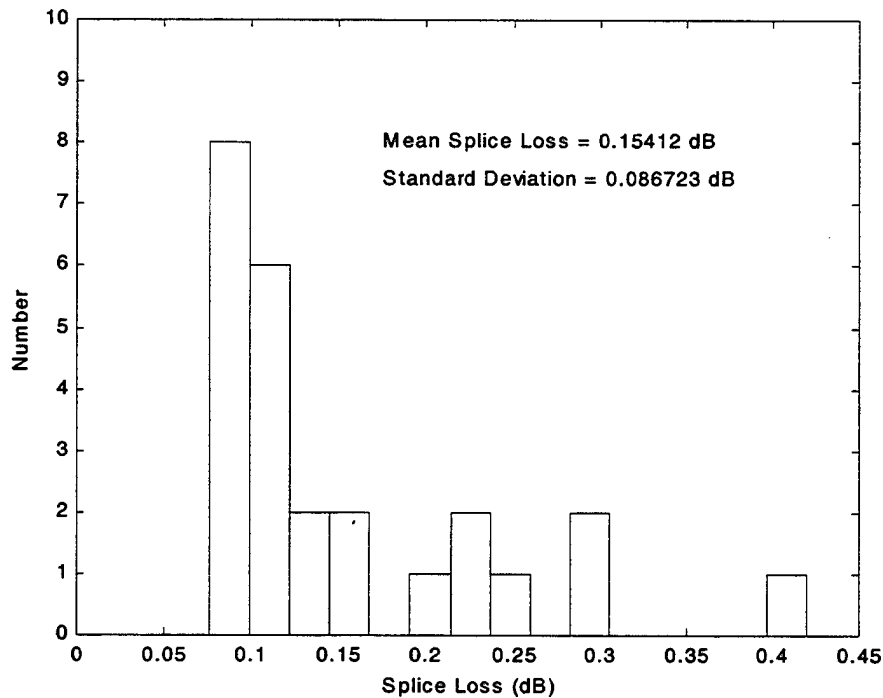


Figure 3.7 Splice Loss Distribution for Multimode Fiber.

Figure 3.8 shows the splice loss distribution for fusion splices using single-mode fiber. The core diameter of the single-mode fiber was 8 μm . Only 15 samples were

obtained before the Sumitomo 11X Splicer experienced a motor failure in its alignment mechanism. The mean splice loss for the single-mode fiber was 0.32 dB. This loss is larger than the multimode fiber in part due to the smaller core diameter. Additionally, the single-mode fiber tested was cabled for outdoor use. The bare fiber was surrounded by eleven metallic wires that act as strengthening members to protect the fiber cable. However, the wires made it difficult to obtain accurate fiber alignments, and small variations in the movement of the fiber would misalign the fiber ends within the V-grooves.

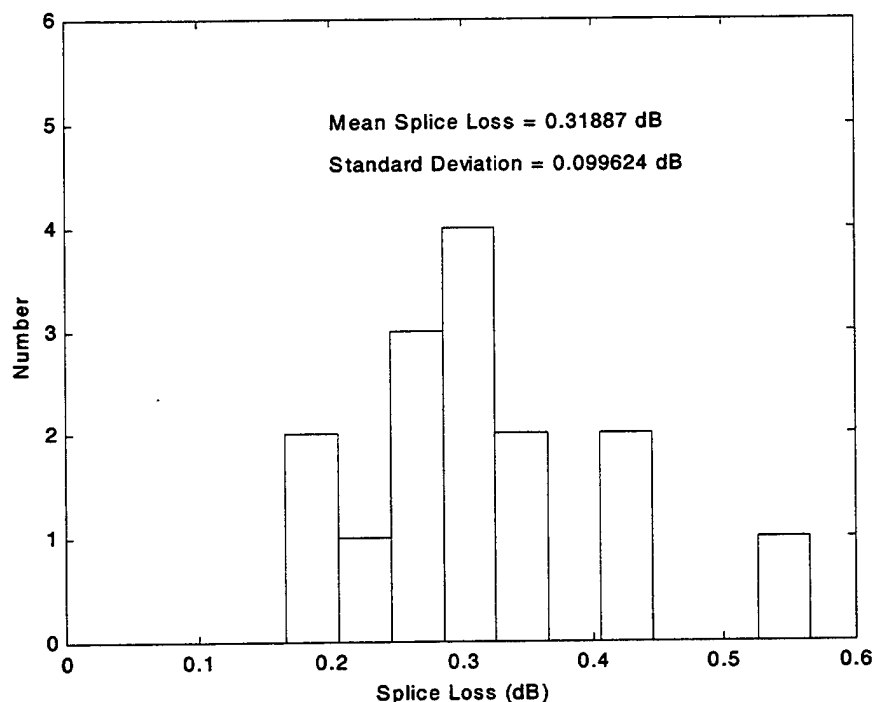


Figure 3.8 Splice Loss Distribution for Single-Mode Fiber.

2. Mechanical Splices

Mechanical splices are less permanent than fusion splices and losses tend to be higher than in fusion splices; typically between 0.2 dB and 0.8 dB. However, they are very useful for temporary experiments where fiber connections need to be made quickly or changed often. Mechanical splices connect two fibers together by clamping them together in a precision housing or by gluing them together. For the $\Sigma\Delta$ modulator, an elastomeric splice was used in the testing of the phase modulator and the semiconductor optical amplifier. The elastomeric splice consists of an outer sleeve surrounding two elastomer members that create a small V-groove in the center. Because the members are made of a flexible material, they squeeze the two fibers into alignment as shown in Figure 3.9. Index matching gel is inserted into the elastomeric splice to reduce reflection losses.

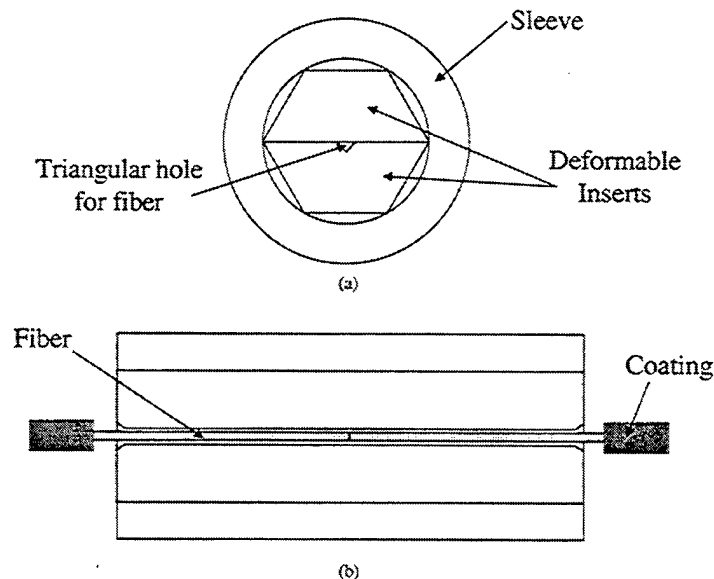


Figure 3.9 (a) Cross-Section View of an Elastomeric Splice (b) Side View of an Elastomeric Splice. From [13].

The experimental results of the elastomeric splices are shown in Figure 3.10. The results show an increase in the splice loss for mechanical splices over fusion splices. The mean loss was 0.97 dB and the variance was 0.15 dB. Because the splice does not physically bond the fibers, proper end preparation and cleaning are critical to avoiding excess losses.

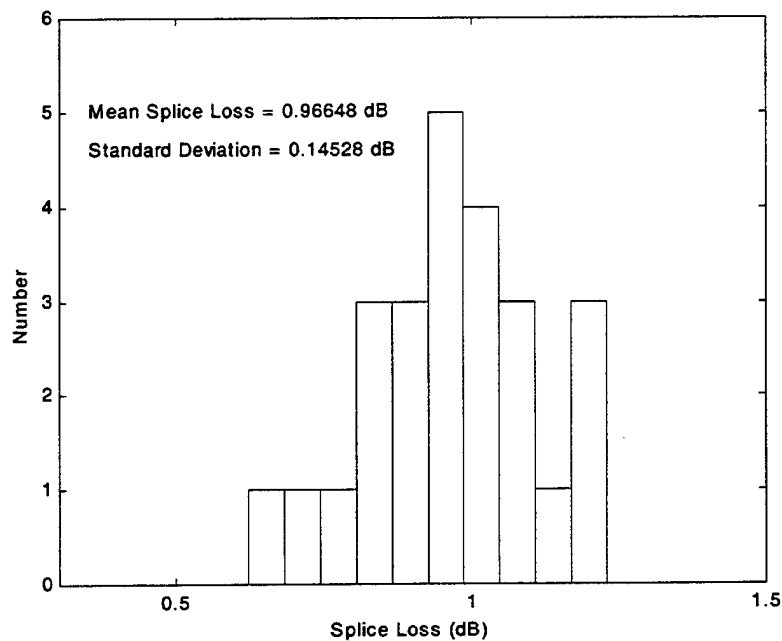


Figure 3.10 Splice Loss Distribution for Elastomeric Splices.

D. WAVEFORM SELECTION

There are two waveforms critical to the design of the electro-optical $\Sigma\Delta$ modulator. The first is the diode laser modulation waveform and the second is the RF antenna voltage waveform. Both waveforms were generated using a Wavetek Function Generator with a maximum deliverable frequency of 20 MHz.

1. Laser Modulation Waveform

Two BCP 400A, 1550-nm Fabry-Perot lasers were tested to determine which would deliver the maximum optical power to the $\Sigma\Delta$ modulator. The peak coupled optical power specified for both lasers is 1 mW [16]. Using the Hewlett Packard 70951B optical spectrum analyzer the power in the peak wavelength of each laser was measured. The maximum power at 1550 nm for unit one was 252 μW and the full wave half-maximum spectral width was 5.05 nm. For the second unit, the maximum power at 1550 nm was 280 μW and the spectral width was 4.37 nm. Since the peak power difference between the two units was only 28 μW , a second optical power measurement was performed. Each laser was connected to a Wavetek function generator and driven first with an Emitter Coupled Logic (ECL) pulse waveform and then an analog square wave with a peak-to-peak voltage of -1.8 volts. In order to be able to display detailed results using the Tektronix 2445B Oscilloscope and the VirtualBench™ computer workstation, a 50 kHz frequency was selected for both the ECL and analog square wave pulses. The results are shown in Table 3.1.

Laser Unit	ECL Pulse	Analog Square Wave
BCP 400A (Unit 1)	93.2 μW	349.5 μW
BCP 400A (Unit 2)	112.5 μW	485.8 μW

Table 3.1 Results of the Laser Drive Waveform Testing.

The ECL pulse waveform delivered less optical power than the analog square wave in both units. However, laser unit two delivered greater optical power than unit one

in each case. This difference is a result of different bias points for each laser unit. In the case of unit two, it emits more optical power using the same drive current than unit one and was selected as the laser system for the $\Sigma\Delta$ modulator. Additionally, the waveform selected to drive the laser was the analog square wave at 50 kHz. The final laser modulation waveform, shown in Figure 3.11, results in a laser pulse train with a pulse-repetition-frequency (PRF) of 50 kHz and a duty cycle of 10 μsec .

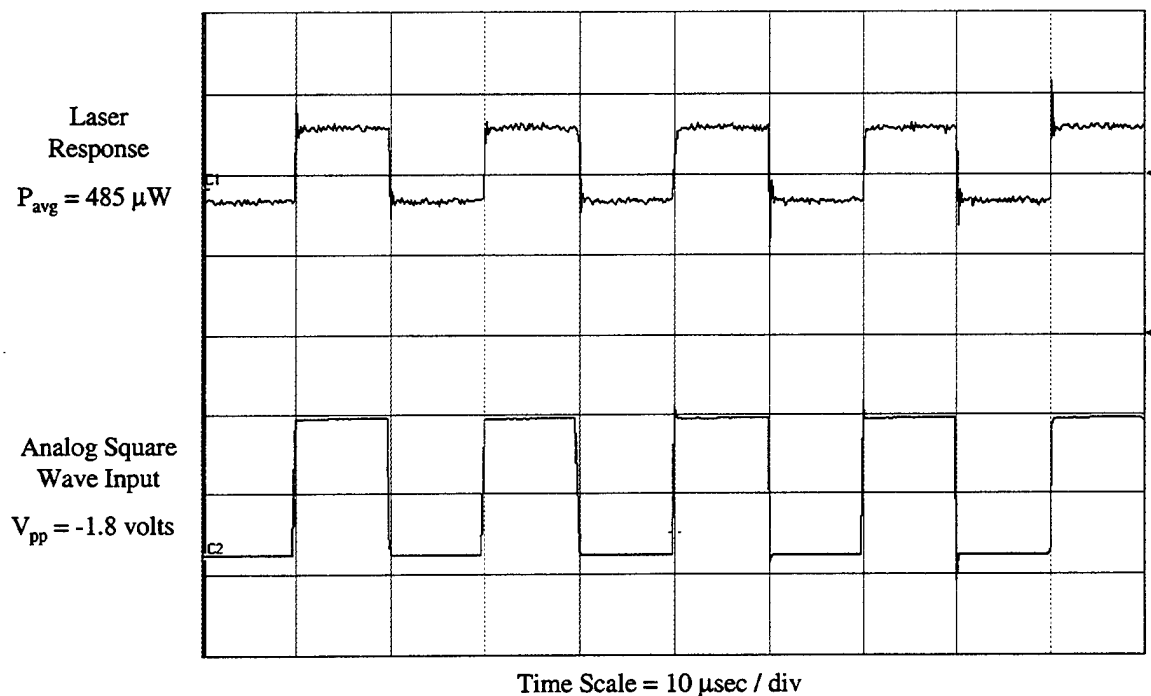


Figure 3.11 Fabry-Perot 1550-nm Laser Drive Signal and Response.

2. RF Antenna Voltage Waveform

Several possible RF antenna voltage waveforms could be selected as inputs to the $\Sigma\Delta$ modulator. However, one key characteristic required of the waveform was a distinct change in the slope of the voltage as it reaches the peak values. Additionally, the voltage slope should gradually change as it moves from peak to peak. This will highlight the

expected transfer characteristics of the interferometers during testing. The waveform must be at a low enough frequency such that it will be oversampled by the 50 kHz laser pulse train by at least a factor of ten. Using these criteria, a 2 kHz triangular waveform was selected as the input to the $\Sigma\Delta$ modulator providing an oversampling ratio (OSR) of 12.5.

E. SIGNAL OVERSAMPLING PATH DESIGN

1. Signal Oversampling Subsystem Operation

In the $\Sigma\Delta$ modulator, the oversampling paths couple the RF antenna voltage into the optical domain. The oversampling paths consist of the 1550-nm diode laser, a 3-dB optical splitter, two polarization controllers, two Mach-Zehnder interferometers (MZIs), two photodetectors, four amplifiers, and one DC power supply. The design layout is shown in Figure 3.12.

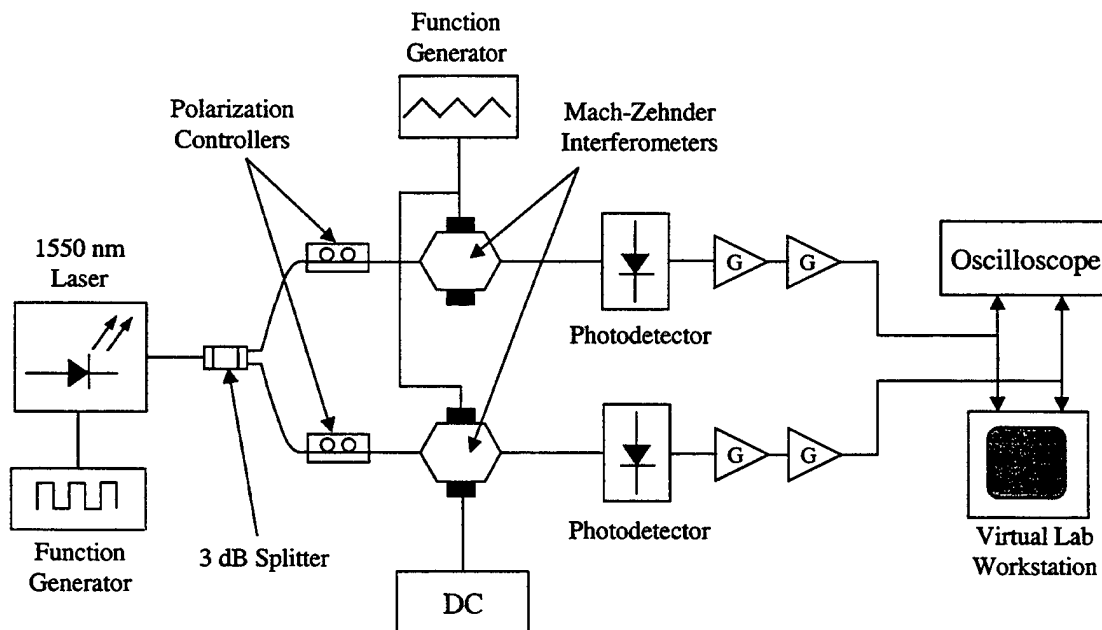


Figure 3.12 Block Diagram of the Signal Oversampling Subsystem.

Light from the 1550-nm diode laser source is pulsed at the sampling frequency. In this case, the sampling frequency is 50 kHz giving an OSR of 12.5. When the light reaches the 3-dB splitter, one-half of the light energy is transferred to the direction path, and the remaining light will be directed to the magnitude path. The light in both the direction and magnitude paths are randomly polarized, yet the input fibers to the MZIs are polarization maintaining (PM) to match the polarization of the MZI waveguides. Therefore, a polarization controller is required in each path just before the location where the single-mode fiber and PM fiber are spliced together. As the pulsed laser light enters each MZI, the optical energy is amplitude modulated by the antenna RF voltage. In this case, the RF antenna voltage is a 2-kHz triangular wave. The modulated light energy from each path is detected by the photodetectors and then amplified before being displayed on the Tektronix 2445B oscilloscope or the VirtualBench™ workstation.

2. Construction of the Signal Oversampling Subsystem

The BCP 400A diode laser was first connected to the Wavetek function generator, and modulated by a -1.8 volt peak-to-peak analog square wave as described in Section D. Next, a 0.45 meter section of 8/125 single-mode fiber with factory installed FC connectors was selected to connect the BCP 400A diode laser and the Newport F-CPL-F22155 3-dB splitter. One of the FC connectors was removed from the single-mode fiber and the end was cleaned and cleaved. Using a Sumitomo Type36 splicer the fiber was fusion spliced to the P1 input (red pigtail) of the 3-dB splitter. Next the P2 output fiber (blue pigtail) of the 3-dB splitter was cleaned and cleaved before splicing it to the polarization maintaining (PM) input fiber of the JDS Uniphase, MZ150-000560 direction

MZI. Likewise, the P3 output fiber (red pigtail) of the 3-dB splitter was cleaned and cleaved before splicing it to the PM input fiber of the JDS Uniphase, MZ150-000560 magnitude MZI. In order to connect the output fibers of the direction and magnitude MZIs to the photodetectors, two 0.65 meter sections of 9/125 single-mode fiber with factory installed FC connectors were selected. One of the FC connectors was removed from each fiber and the ends cleaned and cleaved. These fibers were spliced to the SMF-28 output fibers of the direction and magnitude MZIs. The FC connectors were then attached to the New Focus 1024 high-speed photodetectors. A 50 Ω impedance-matched cable was connected to the output of each photodetector. Because the New Focus 1024 photodetectors lack internal amplifiers, two Hewlett Packard 461A amplifiers were connected in series to the output of the direction and magnitude path photodetectors. This amplification was necessary to display the output voltage signals on the Tektronix 2445B oscilloscope and the VirtualBench™ workstation.

To apply the RF antenna voltage to the magnitude and direction MZIs, a second Wavetek function generator was connected to the SMA inputs of the MZIs. This Wavetek supplied the 2-kHz triangular waveform to the RF ports of the MZIs. Additionally, a DC voltage supply was connected to the DC bias port of the magnitude MZI. This DC voltage supply provided the $+V_{\pi}/2$ voltage required to bias the transfer function of the magnitude MZI such that it is $\pi/2$ radians out of phase with the direction MZI transfer function.

F. COMPARATOR CIRCUIT DESIGN

The LM319 comparator circuit delivers an appropriate voltage, σ , to the input of the phase modulator. The circuit design is shown in Figure 3.13. If the direction path voltage, V_{in} , exceeds the threshold value of the comparator circuit, V_T , the output of the circuit is 0 volts. If V_{in} is less than V_T , the comparator circuit outputs 4.0 volts to apply the proper phase delay in the phase modulator. The circuit utilizes an inverted architecture because the operation of the phase modulator necessitates a value of 0 volts when the direction path input voltage is in the high state. The reference voltage is stabilized by a 5-volt regulator and determined by a voltage divider circuit. All resistors are rated for a 1% tolerance.

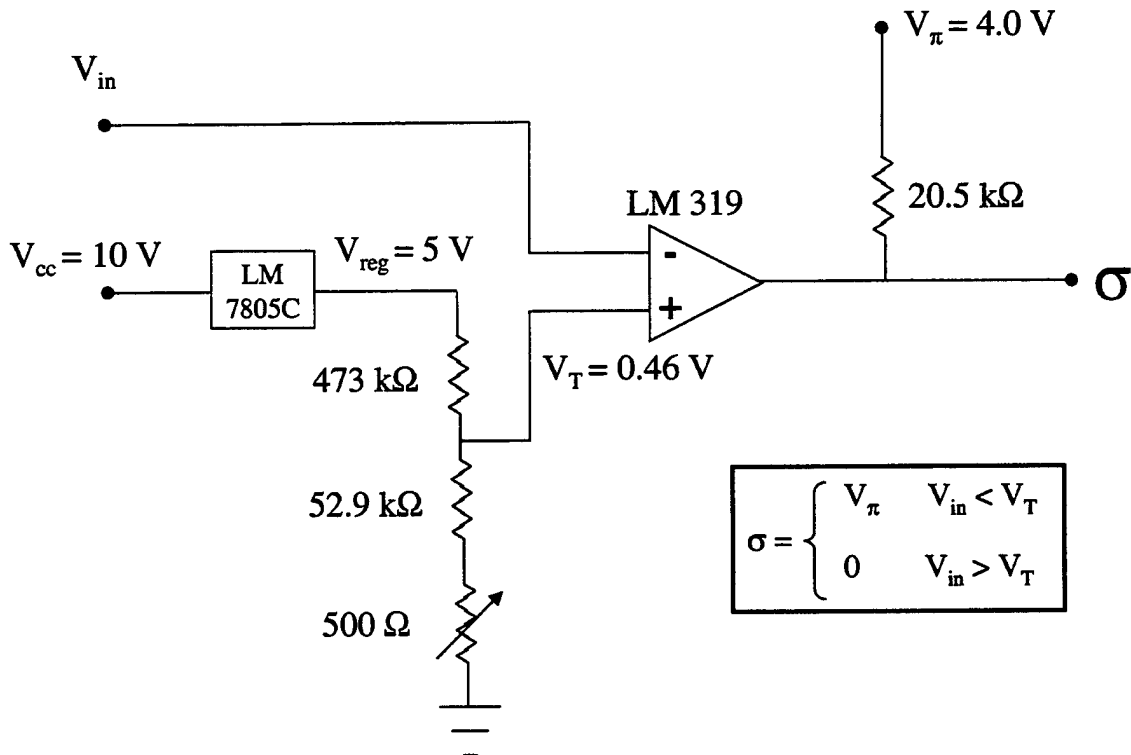


Figure 3.13 Direction Path Comparator Circuit.

A ten-turn 500 Ω potentiometer is added to the voltage divider to allow for adjustments in the reference voltage due to drift. The output of the comparator circuit utilizes a DC power supply set at 4.0 volts in conjunction with a 20.5 k Ω pull-up resistor.

G. FIBER LATTICE ACCUMULATOR DESIGN

The fiber lattice accumulator is the most critical of all the designed and fabricated components within the electro-optical $\Sigma\Delta$ digital antenna. It is a phase coherent device and consists of a phase modulator, two directional couplers, a semiconductor optical amplifier, and a length of fiber that creates the optical delay. The block diagram of the configuration for the fiber lattice is shown in Figure 3.14. The blocks A_0 and A_1 are the directional couplers, the optical fiber delay, which is equal to $1/\text{PRF}$ of the pulsed laser, is represented by the z^{-1} block, and the semiconductor optical amplifier is represented by G .

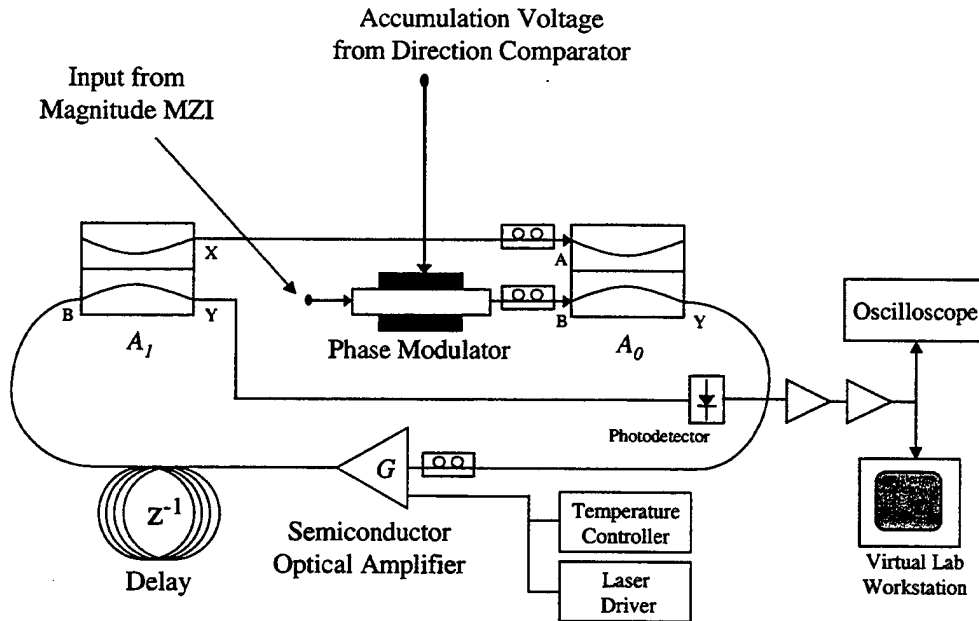


Figure 3.14 Block Diagram of the Fiber Lattice Accumulator.

The first consideration in the design of the fiber lattice accumulator was the choice of the oversampling frequency and the RF antenna voltage input frequency. Because the accumulation of the optical pulse occurs via coherent recirculation in the fiber lattice, the optical delay of each pulse in the fiber lattice must be one pulse repetition interval (PRI). If the oversampling frequency of 50 kHz in the design of the signal sampling subsystem were used, the required delay would be on the order of 20 μ sec. To achieve this delay approximately 4083.80 meters of fiber would need to be incorporated into the design of the fiber lattice accumulator. However, long lengths of fiber present a challenge because of dispersion and attenuation. As a pulse of light travels through single-mode fiber it experiences a spreading in the time domain caused by material dispersion and waveguide dispersion [12]. The spreading determines the separation between two adjacent pulses. If the dispersion is significant, inter-symbol interference between two pulses could occur in the fiber lattice accumulator. This would have a negative effect as the accumulation in the fiber lattice is based on the coherent interference of distinct pulses in the A_0 directional coupler. Attenuation decreases the power in the optical signal exponentially as the length of fiber increases. This attenuation is wavelength dependent and also depends upon the material of the fiber and the amount of impurities in the fiber [12].

To minimize the potential problems caused by dispersion and attenuation, the oversampling and the RF antenna voltage input frequencies were increased to 200 kHz and 8 kHz respectively. The oversampling ratio for the system remained at 12.5. By

increasing the oversampling and RF antenna voltage frequencies, the length of fiber required in the fiber lattice delay decreased from 4083.80 meters to 1020.95 meters.

In order to determine the length of additional fiber needed in the feedback path of the fiber lattice accumulator, the lengths of the fiber pigtails used in the construction of the fiber lattice were measured and subtracted from the 1020.95 meter delay loop. The pigtails included in the construction of the fiber lattice were the input and output pigtails of the A_0 directional coupler, the semiconductor optical amplifier, and the A_1 directional coupler. The total length of the pigtails was 8.45 meters leaving 1012.50 meters required to form the additional pulse delay in the feedback path.

To begin construction of the fiber lattice, the output of the magnitude MZI was spliced to the input of the phase modulator. Because the phase modulator is a polarization dependent waveguide, a polarization controller was placed just before the location of the splice between the magnitude MZI and phase modulator. The output of the direction comparator circuit was connected to the RF input port on the phase modulator. This connection drives the phase modulator with the correct voltage for accumulation up or accumulation down in the fiber lattice.

Next, the output of the phase modulator was spliced to the B input fiber of the A_0 directional coupler. It is at the A_0 directional coupler where the coherent constructive or destructive interference occurs within the fiber lattice. The Y output of the A_0 directional coupler was spliced to the input fiber of the semiconductor optical amplifier to provide the recirculation and amplification of the optical signal. The output of the semiconductor

optical amplifier was spliced to the B input of the A_1 directional coupler. The A_1 directional coupler acts as a splitter directing part of the optical energy to the output of the fiber lattice and part of the optical energy through the feedback path to the A_0 directional coupler.

To complete the feedback path from the A_1 directional coupler to the A_0 directional coupler, the 1012.50 meter delay loop was constructed. This delay loop consisted of two 500-meter spools of SMF-28 single-mode fiber spliced together and 12.5 meters of SMF-28 single-mode fiber from a third spool. The input fiber to the delay loop was spliced to the X output fiber of the A_1 directional coupler, and the output fiber of the delay loop was spliced to the A input fiber of the A_0 directional coupler.

The final step in the construction of the fiber lattice was the addition of three polarization controllers. The first two polarization controllers were added to the A and B input fibers of the A_0 directional coupler. The A_0 directional coupler acts as a combiner for the optical signals from the phase modulator and the feedback path, and in order to combine properly the polarization relationships must be maintained. The third polarization controller was placed just before the input to the semiconductor optical amplifier. Because semiconductor optical amplifiers have different crystal planes in the gain medium, they are also polarization dependent [17].

H. SUMMARY

The construction process for each of the critical elements in the NPS electro-optical $\Sigma\Delta$ modulator has been presented. Construction began with a thorough

characterization of the fiber splicing process used to connect the different optical components. The characteristics required of the sampling laser waveform and the RF antenna voltage waveform were determined, and proper modulation of the sampling laser was verified. Next, the signal oversampling subsystem and the direction comparator circuit were assembled. Finally, the fiber lattice accumulator was constructed and connected to the output of the signal oversampling subsystem. Understanding the development and construction of each of these elements was instrumental in developing the test and evaluation of the electro-optical $\Sigma\Delta$ modulator.

IV. MEASUREMENTS OF THE NPS ELECTRO-OPTICAL, SIGMA-DELTA MODULATOR

A. OPTICAL POWER LOSS MEASUREMENTS

One of the design considerations during the construction of the electro-optical $\Sigma\Delta$ modulator was to minimize the optical losses in the signal oversampling subsystem and the fiber lattice structure. The maximum optical power delivered by the pulse modulated 1550-nm laser source was 485.8 μW . The photodetectors used in the construction of the electro-optical $\Sigma\Delta$ modulator have a rated noise equivalent power (NEP) of 45 $\text{pW}/\text{Hz}^{1/2}$ and a bandwidth (B_w) of 50 kHz. In order to achieve a signal-to-noise ratio (SNR) equal to one at the detectors, the received power must equal $\text{NEP} \cdot (B_w)^{1/2}$. For these photodetectors, this received power is 10 nW. If it assumed the received power must be 10 dB larger in order to maintain a specified bit error ratio, the received power becomes 0.1 μW . The acceptable loss within the $\Sigma\Delta$ modulator is $10 \cdot \text{Log}(485.8 \mu\text{W} / 0.1 \mu\text{W})$, or 36.9 dB. A power budget was established to determine the theoretical losses in the signal oversampling subsystem and in the system as a whole. This budget was then compared with the measured optical losses and to the total acceptable loss to determine if modifications needed to be made.

There are many sources of optical loss in a fiber system. Large insertion losses are associated with integrated optical devices such as Mach-Zehnder interferometers (MZIs) and phase modulators. Other losses are incurred at the connectors and the junctions of fusion splices and couplers.

1. Signal Oversampling Subsystem Optical Loss

Table 4.1 below specifies the calculated and measured power budget for the signal oversampling subsystem. It includes the input power from the BCP 400A diode laser source and losses from fusion splices, connectors, the 3-dB coupler and the MZIs.

Direction Path			Magnitude Path		
Item	Loss (dB)	Power (dBm)	Item	Loss (dB)	Power (dBm)
BCP Laser		-3.135	BCP Laser		-3.135
FC Connector	0.300		FC Connector	0.300	
Splice	0.319		Splice	0.319	
3-dB Splitter	3.170		3-dB Splitter	3.070	
Splice	0.090		Splice	0.150	
MZI	3.900		MZI	3.800	
Splice	0.140		Splice	0.100	
FC Connector	0.150		FC Connector	0.310	
Total Loss	8.069		Total Loss	8.049	
Calculated Output Power		-11.204	Calculated Output Power		-11.184
Measured Output Power		-12.291	Measured Output Power		-13.143

Table 4.1 Power Budget for the Signal Oversampling Subsystem.

In the case of the direction path, the calculated output power is close to the measured output power. The additional 1.087 dB loss can be attributed to absorption loss, scattering loss and bending loss [12]. In the magnitude path, the calculated output

power is greater than the calculated output power of the direction path, yet the measured output power was less than the measured output power of the direction path. The additional 1.959 dB loss, which corresponds to a loss of 27.5 μ W, could be associated with a high-loss splice or a misalignment on one of the connectors. A check of the system could not locate the specific source of the additional loss. However, the additional loss was not a major concern as the sensitivity of the photodetectors is sufficient to handle the measured power in the magnitude path.

2. The Electro-Optical, Sigma-Delta Modulator Optical Loss

In order to determine the optical loss of the entire system, the measured and estimated losses were captured in a table in the order in which they occur in the system. Table 4.2 shows the power delivered into the electro-optical $\Sigma\Delta$ modulator by the BCP 400A laser, the insertion loss of each of the integrated optical devices, the estimated splice losses, the measured FC connector losses, and the gain of the semiconductor optical amplifier (SOA). At the bottom of the table is the calculated output power and the measured output power of the electro-optical $\Sigma\Delta$ modulator.

A straight-forward approach to calculating the optical loss in the electro-optical $\Sigma\Delta$ modulator was not possible due to the feedback loop within the fiber lattice accumulator. Light power from the feedback loop combines with the light power from the phase modulator at the A_0 directional coupler with each iteration through the fiber lattice accumulator. Eventually, however, the output of the A_0 directional coupler will converge to a fixed value. In order to calculate the output power of the $\Sigma\Delta$ modulator, a MATLAB program was created using the data in Table 4.2 to simulate the recirculation

of the optical power within the fiber lattice accumulator. The result converged in only eleven iterations to an output power of -11.024 dBm, or $79.0 \mu\text{W}$.

Item	Loss (dB)	Power (dBm)
BCP Laser		-3.135
FC Connector	0.300	
Splice	0.319	
3-dB Splitter	3.070	
Splice	0.319	
Magnitude MZI	3.800	
Splice	0.120	
Phase Modulator	2.200	
Splice	0.190	
A0 Directional Coupler	3.000	
Splice	0.010	
SOA	-6.020 (gain)	
Splice	0.100	
A1 Directional Coupler	3.000	
Output Splice	0.020	
Output FC Connector	0.310	
Feedback Delay Path	0.220	
Calculated Output Power		-11.024
Measured Output Power		-10.590

Table 4.2 Power Budget for the Electro-Optical $\Sigma\Delta$ Modulator.

In order to measure the output power of the electro-optical $\Sigma\Delta$ modulator, the BCP 400A diode laser source was modulated using a 200-kHz square wave. The

directional couplers in the fiber lattice were set to their 3-dB coupling ratios and the gain of the SOA was set at 6.02 dB. The output of the fiber lattice was connected to an optical multimeter in order to record the output power. The result was a measured output power for the $\Sigma\Delta$ modulator of -10.88 dBm, or 81.7 μ W.

The difference between the calculated output power and the measured output power of the $\Sigma\Delta$ modulator is only 0.434 dB. In fact, the calculated power is slightly less than the measured output power. Based on the calculated and measured output power results, the optical power loss in the electro-optical $\Sigma\Delta$ modulator is at an acceptable level for experimental testing.

B. SIGNAL OVERSAMPLING SUBSYSTEM MEASUREMENTS

To determine proper operation of the signal oversampling subsystem, several of the signal waveforms were measured at the output of the subsystem under different initial conditions. The first check of the subsystem was to determine that the Mach-Zehnder interferometers properly amplitude-modulate the RF input voltage. For this test, the BCP 400A diode laser source was not modulated with the 50-kHz pulse train, but remained in continuous-wave operation. The RF antenna voltage input was a 2-kHz triangular wave as described in Chapter III. No DC bias was applied to the magnitude MZI, so both the direction and magnitude MZI transfer functions were biased at the same reference point. This reference point for the unbiased MZIs is at the 0.5 relative output intensity point (in other words, with no external bias to the MZI, the light intensity output is one-half the light intensity input). The output of both the direction and magnitude MZIs is shown in Figure 4.1. As expected, the excited waveform of the direction path is π radians out of

phase with the modulated waveform of the magnitude path. This is a result of the coupling mechanism which advances the odd mode of the electric field of the light pulse by $\pi/2$ radians over the even mode of the electric field in the 3-dB coupler and again by $\pi/2$ radians in the MZI [15]. Note that the excited waveform from the direction path is greater in amplitude than the waveform from the magnitude path. Because the magnitude path experiences 0.872 dB more optical loss, less light reaches the photodetector and a smaller amplitude voltage signal is delivered.

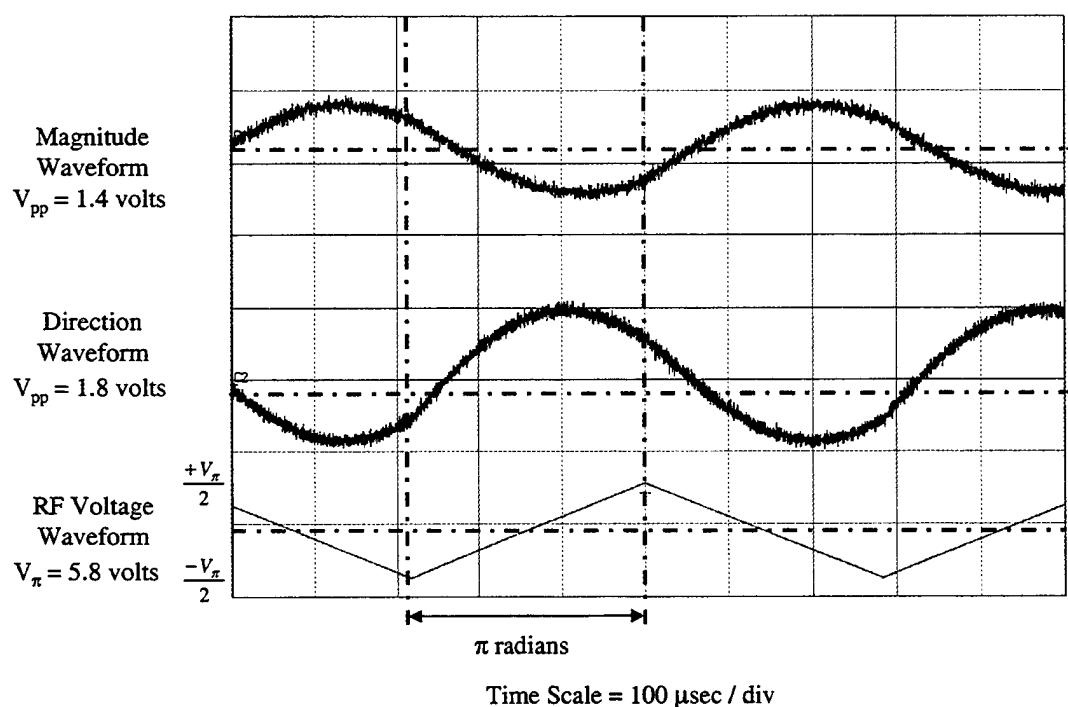


Figure 4.1 Magnitude and Direction Path Waveforms from the Signal Oversampling Subsystem.

In the second experiment, the 1550-nm laser source was amplitude modulated by a 50-kHz sampling pulse waveform as described in Chapter III. This provided the optical

pulse used to oversampled the RF antenna input voltage. The results of this test are shown in Figure 4.2.

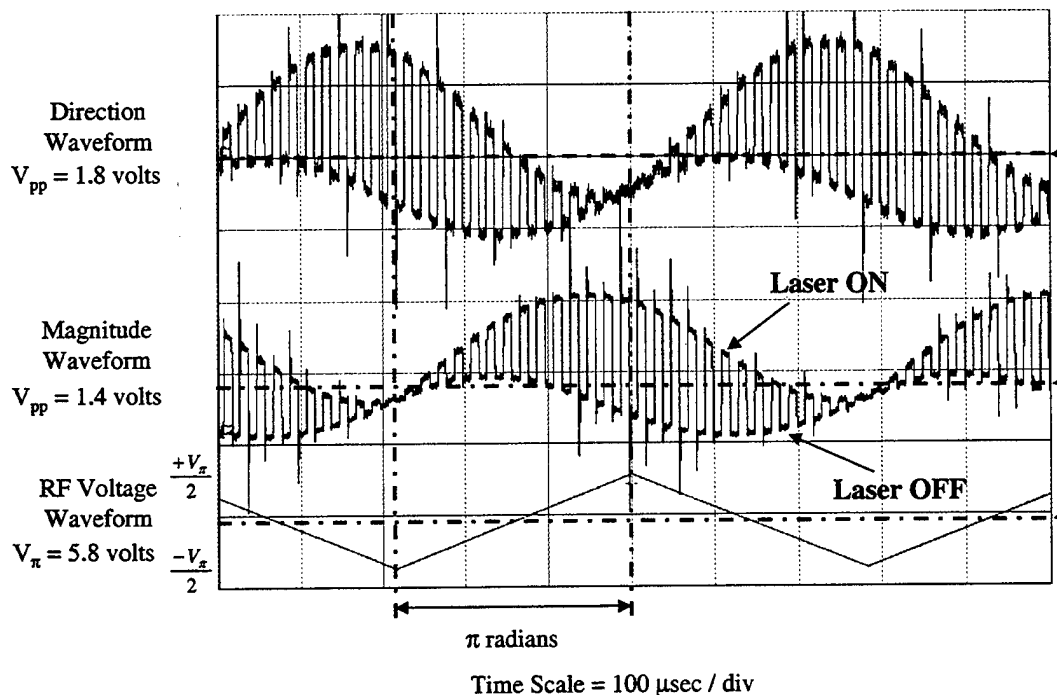


Figure 4.2 Oversampled Waveforms in the Direction and Magnitude Paths.

As in the first experiment, the direction and magnitude waveforms are π radians out of phase with each other as expected. In both cases, when the laser is in the OFF state there is a residual amplitude modulation of the RF voltage waveform. This residual modulation is due to the low extinction ratio of the laser source used in the experiment. The extinction ratio stated in the user manual for the BCP 400A Fabry-Perot laser is 10 dB [16]. In other words, the difference between the light energy delivered in the ON state versus the OFF state is separated by only a factor of ten. Light energy is still emitted when the laser is in the OFF state and this residual light energy is modulated by the RF antenna input voltage.

The next experiment of the signal oversampling system was to determine the response of the MZIs when the RF antenna input voltage exceeds $\pm V_{\pi}/2$. For this test, the 2-kHz triangular wave peak-to-peak voltage was increased from 5.8 volts to 6.6 volts. The resulting waveform for the direction MZI is shown in Figure 4.3.

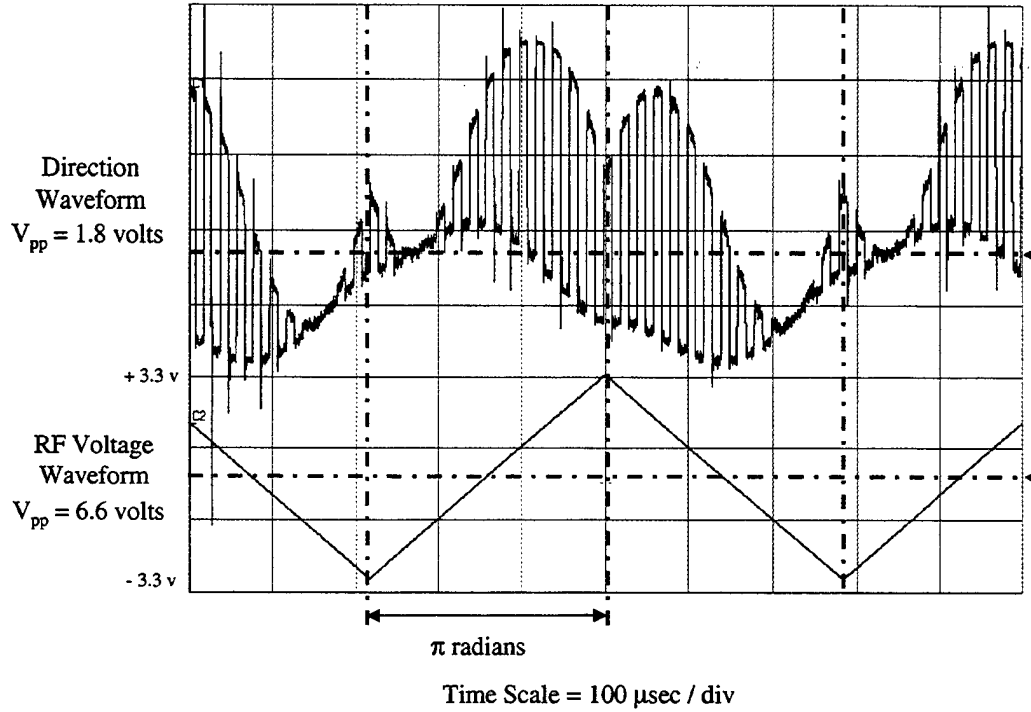


Figure 4.3 Direction MZI Waveform Exhibiting Folding.

The resulting waveform of the direction MZI shows evidence of folding at the peak values of the RF antenna voltage waveform. The same effect was exhibited by the magnitude MZI and confirms the V_{π} value of 5.8 volts given in the manufacturer's specification sheet [18]. This waveform folding is an undesirable condition for the signal oversampling subsystem and can be controlled by limiting the RF antenna input voltage to values between $\pm V_{\pi}/2$.

The final experiment of the signal oversampling subsystem was to bias the magnitude MZI such that its characteristic transmissivity function was $V_\pi/2$ volts out of phase with respect to the direction MZI transmissivity function. Using a computer simulation, Bewley [7] showed the magnitude and direction transmissivity functions should appear as in Figure 4.4. The normalized output intensity of the direction MZI should be zero at $-V_\pi/2$ volts and one at $+V_\pi/2$. The normalized output intensity of the magnitude MZI should be 0.5 at both $-V_\pi/2$ volts and $+V_\pi/2$.

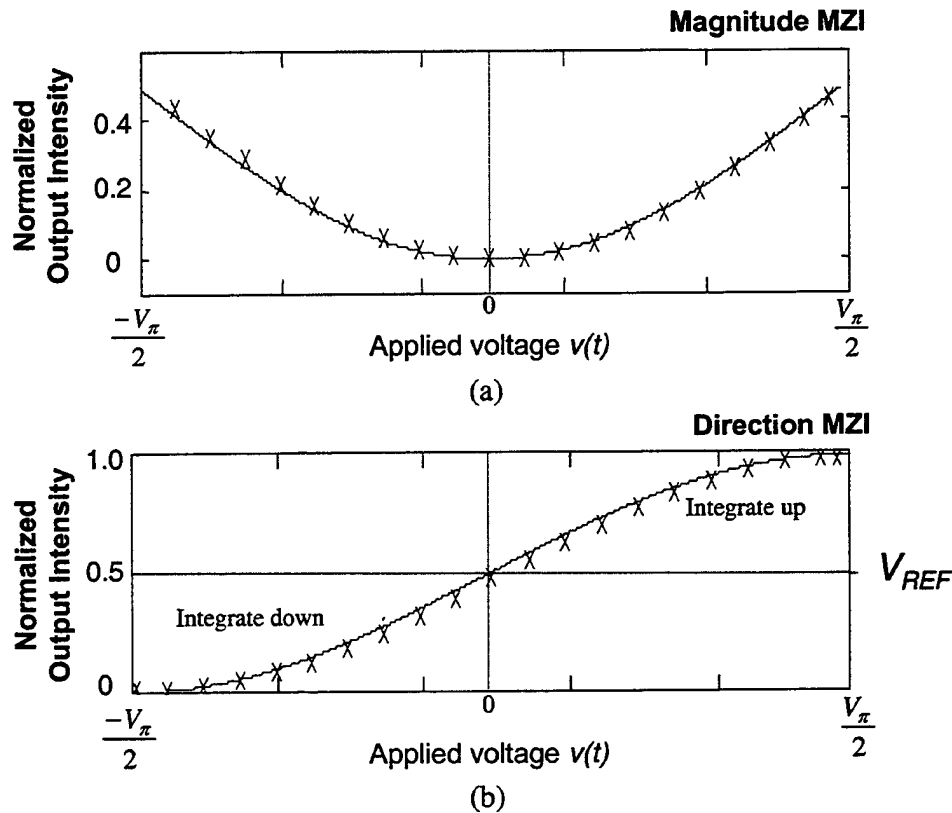


Figure 4.4 Normalized MZI Transmissivity as a Function of the Applied Voltage for (a) The Magnitude MZI and (b) The Direction MZI. [7].

It is the difference in the bias of the MZIs that eliminates the ambiguity in determining the proper accumulation direction within the fiber lattice. If the normalized intensity, or equivalently the photodetector output voltage, of the direction MZI is above the threshold of the comparator circuit, V_T , then the magnitude path light pulse is allowed to pass into the fiber lattice accumulator in-phase. This allows the light energy in the fiber lattice to accumulate up. If, however, the photodetector voltage is below V_T , then the phase modulator will pass the light energy into the fiber lattice accumulator out-of-phase. This will force the light energy in the fiber lattice to accumulate down.

The setup for this experiment required very few changes to the signal oversampling subsystem. The only modification was the addition of a DC power supply connected to the DC bias port of the magnitude MZI. The voltage of the power supply was set at $+V_\pi/2$. According to the manufacturer's specification sheet, this corresponded to +2.9 volts [18].

The oversampling subsystem voltage waveforms of the magnitude and direction paths are shown in Figure 4.5. The measured transmissivity functions for the magnitude and direction MZIs and the RF input waveform are shown in Figure 4.5 (a). For comparison, the theoretical transmissivity functions determined by the computer simulation are shown in Figure 4.5 (b). When the RF input waveform was at $-V_\pi/2$ and $+V_\pi/2$ volts, the magnitude path output voltage was at its maximum. For the direction path, the output voltage was at its minimum when the RF input waveform was at $-V_\pi/2$ and at its maximum when the RF input waveform was at $+V_\pi/2$. The measured

transmissivity functions of the magnitude and direction MZIs qualitatively correspond to the theoretical transmissivity functions described in the computer simulation.

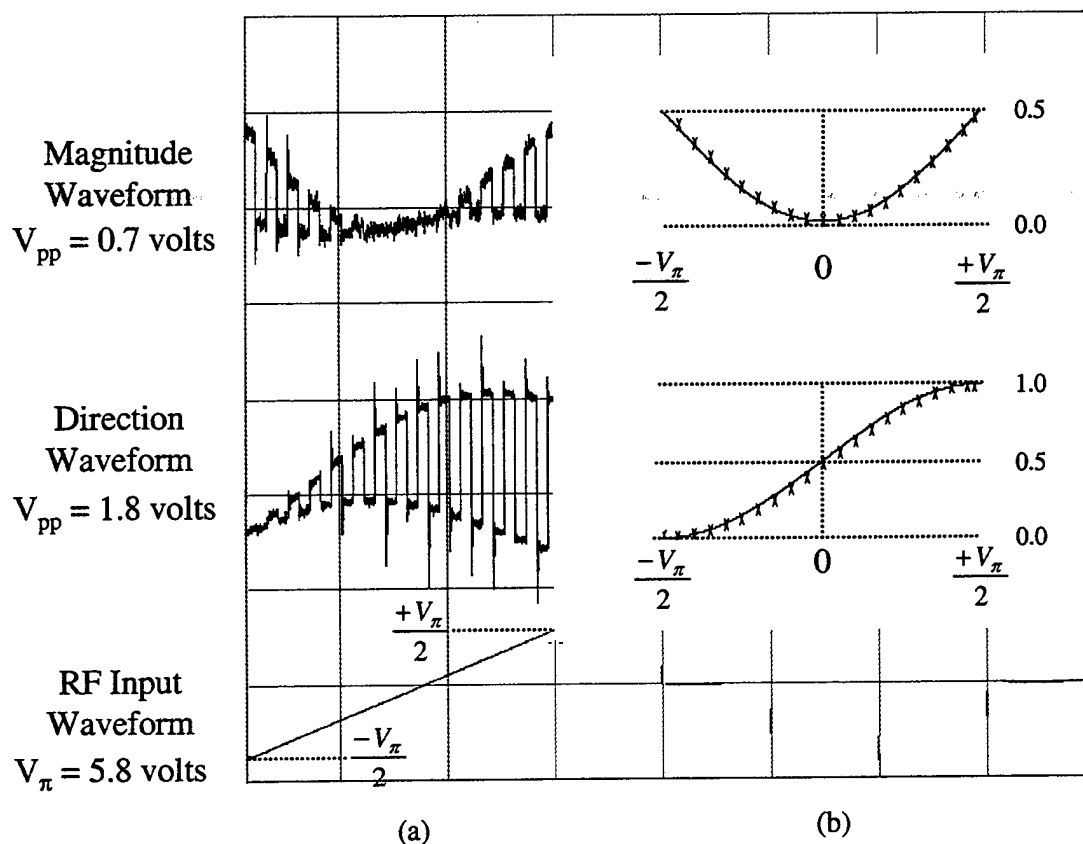


Figure 4.5 (a) Voltage Waveforms of the Magnitude and Direction MZIs. (b) The Normalized MZI Transmissivity for the Magnitude and Direction MZIs as Determined by Computer Simulation.

C. COMPARATOR CIRCUIT MEASUREMENTS

The light energy in the direction path of the signal oversampling subsystem determines the direction of accumulation within the fiber lattice accumulator. In order to determine the correct accumulation direction, a comparator circuit is used to analyze the direction path output voltage. As discussed in Chapter III, the comparator circuit takes

the output voltage of the direction path photodetector as the input and outputs either 0 volts or V_{π} . In this case, V_{π} is 4.0 volts [19].

For this experiment, the laser source was again modulated with the 50-kHz drive signal and the RF antenna input voltage was a 2-kHz triangular wave. The output voltage of the direction path photodetector was amplified by two Hewlett Packard 461A amplifiers in series to provide approximately 30 dB of gain. This voltage was the input to the comparator circuit. The reference voltage, V_T , for the comparator circuit was set by the voltage divider to be 0.46 volts. This reference voltage is required to offset the amplified DC bias of the photodetector. The output of the comparator circuit was supplied by a DC power supply set at 4.0 volts. The output of the direction path MZI and the output of the comparator circuit were displayed on the Tektronix 2445B oscilloscope and the VirtualBench™ workstation. The resulting waveforms are shown in Figure 4.6.

When the output voltage of the direction path was below the voltage threshold of the comparator circuit, the comparator circuit output a constant 4.0 volts. This occurred when a light pulse from the direction path did not have sufficient energy to exceed the comparator threshold. However, when the output voltage of the direction path was above the voltage threshold, the result was an oscillation between 0 volts and 2.2 volts. In this case, a light pulse with sufficient energy temporarily exceeded the voltage threshold of the comparator circuit. Because the output of the direction MZI is amplitude-modulated by the source laser, the voltage output in the direction path dropped below the comparator threshold before the next light pulse reached the photodetector and comparator circuit.

Because of the simple design of the comparator circuit and the way in which the RF signal is amplitude-modulated by the direction MZI, each crossing of the comparator threshold into the high state is followed by another crossing into the low state.

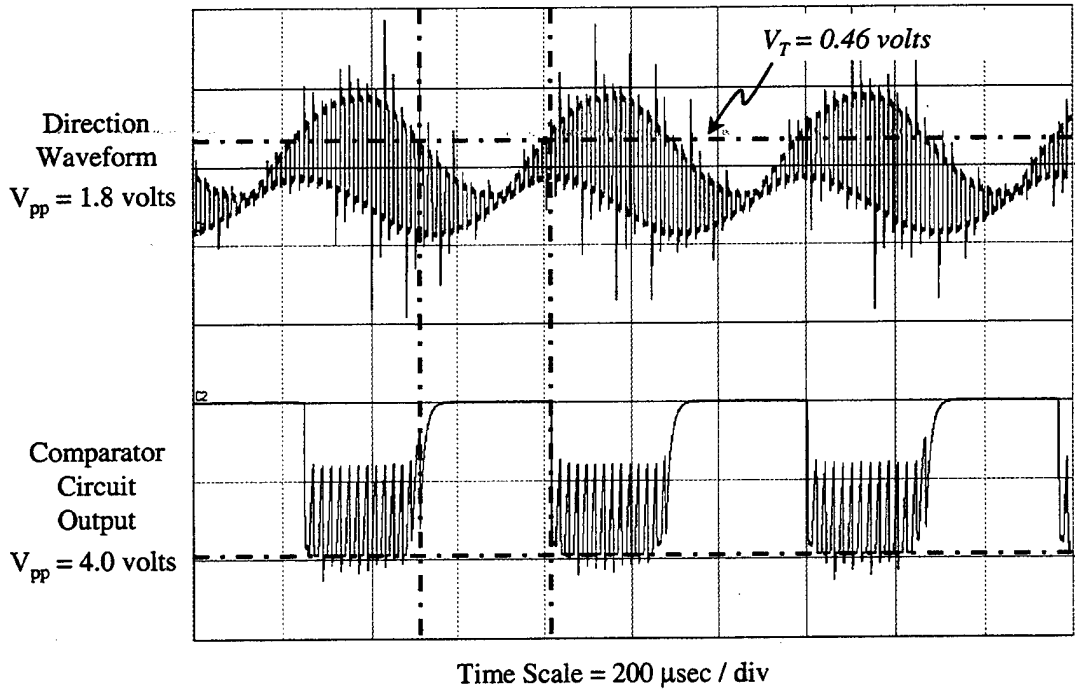


Figure 4.6 Voltage Output of the Direction Comparator Circuit Compared to the Direction Path Waveform.

However, this behavior is not expected to adversely affect the overall performance of the electro-optical $\Sigma\Delta$ modulator. When a light pulse of sufficient energy from the direction path exceeds the comparator threshold, the output to the phase modulator is 0 volts. When that light pulse has passed through the phase modulator, the output voltage of the direction path drops below the threshold and the comparator circuit responds, sending a maximum of 2.2 volts to the phase modulator. However, when this occurs, the next light pulse from the magnitude path has not yet reached the phase modulator.

D. PHASE MODULATOR CHARACTERIZATION

The phase modulator is an electro-optic device important to coherent communications. In a phase modulator, an applied electric field changes the refractive index in a titanium diffused, single-mode waveguide. This applied field can then be used to create a variable delay of the optical wave [15]. Because the delay of the optical wave is on the order of half a wavelength or less, traditional methods of determining phase delay cannot be used. To characterize the phase modulator, a test was devised to simulate the operation of a Mach-Zehnder interferometer (MZI). The ratio of the output intensity to the input intensity, also called the transmissivity, of an MZI is a function of the phase delay experienced by the phase modulator, given by

$$H_{MZI} = \frac{I_{OUT}}{I_{IN}} = \frac{1}{2} + \frac{1}{2} \cos[\Delta\phi(V)], \quad 4.1$$

where I_{OUT} and I_{IN} are the output and input light intensities of the MZI. The phase difference of the light wave is $\Delta\phi(V)$ and is a function of the input voltage, V , to the phase modulator. The transmissivity can also be rewritten as

$$H_{MZI} = \frac{I_{OUT}}{I_{IN}} = \cos^2 \left[\frac{\Delta\phi(V)}{2} \right]. \quad 4.2$$

The phase difference in the phase modulator is represented by

$$\Delta\phi(V) = \frac{\pi n_e^3 r_{33} \Gamma L_i V(t)}{G \lambda_L}, \quad 4.3$$

where n_e is the index of refraction of the optical waveguide, r_{33} is the linear electro-optic coefficient, Γ is the electro-optic overlap parameter, L_i is the electrode length, G is the inter-electrode gap, and λ_L is the wavelength of the laser. For a phase difference of π radians the voltage, $V(t)$, required is called V_π and is given by

$$V_\pi = \frac{G\lambda_L}{n_e^3 r_{33} \Gamma L_i}. \quad 4.4$$

The configuration used to characterize the phase modulator is shown in Figure 4.7. Continuous-wave light energy from a BCP 400A laser source was directed into a 3-dB splitter. Half of the light energy traveled through one arm of the interferometer without experiencing a delay. The other half of the light energy traveled through the second arm and passed through the phase modulator. The phase modulator was excited by a triangular wave with a voltage from $-V_\pi/2$ to $+V_\pi/2$. The V_π value specified by the manufacturer was 4.0 volts [19]; therefore, the triangular wave was set from -2.0 volts to 2.0 volts. As the input voltage to the phase modulator moved from peak-to-peak, the light wave in the second arm experienced a delay from zero to $\lambda/2$. The light energy from both arms was recombined at a 3-dB combiner. Because coherent interference was required, three polarization controllers were used, one at the input to the phase modulator and two on each arm of the interferometer just before the 3-dB combiner. Finally, the light energy from the combiner was delivered to a photodetector that output a voltage

proportional to the light energy received. This voltage signal was amplified and displayed on a Tektronix 2445B oscilloscope and a VirtualBench™ workstation.

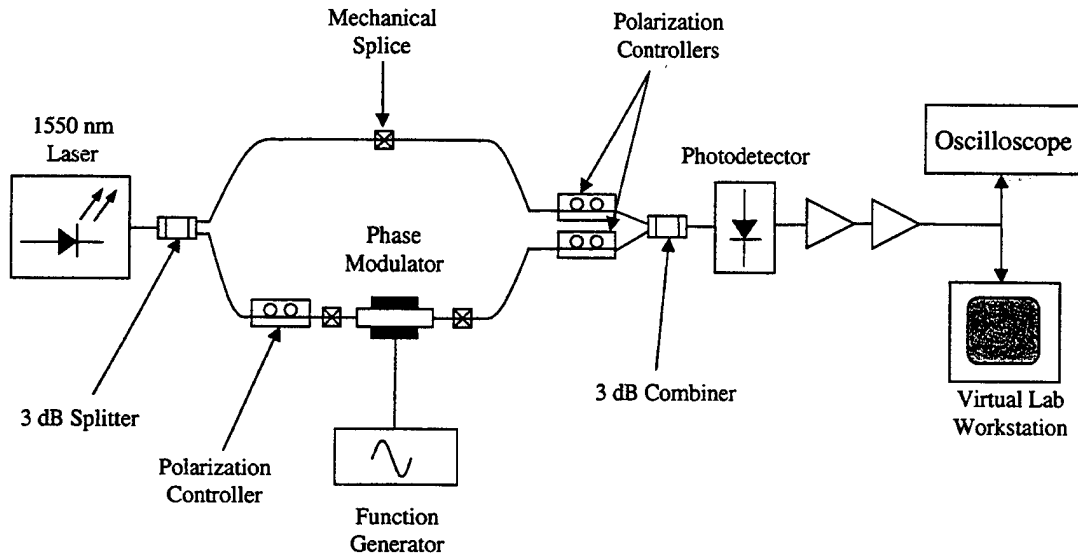


Figure 4.7 Block Diagram of the Phase Modulator Characterization Test.

The results of the characterization test are shown in Figure 4.8. The output voltage conforms to a cosine squared wave as expected from Equation 4.2 (The noise that appears with the output waveform is an artifact of the amplifiers and the system noise in the circuit). The voltage output of the photodetector was on the order of 10 μ volts. When the signal was amplified to the display voltage ($V_{pp} = 10$ mv), the system noise was amplified as well. From this experiment, the value of V_{π} was confirmed to equal 4.0 volts as described by the manufacturer.

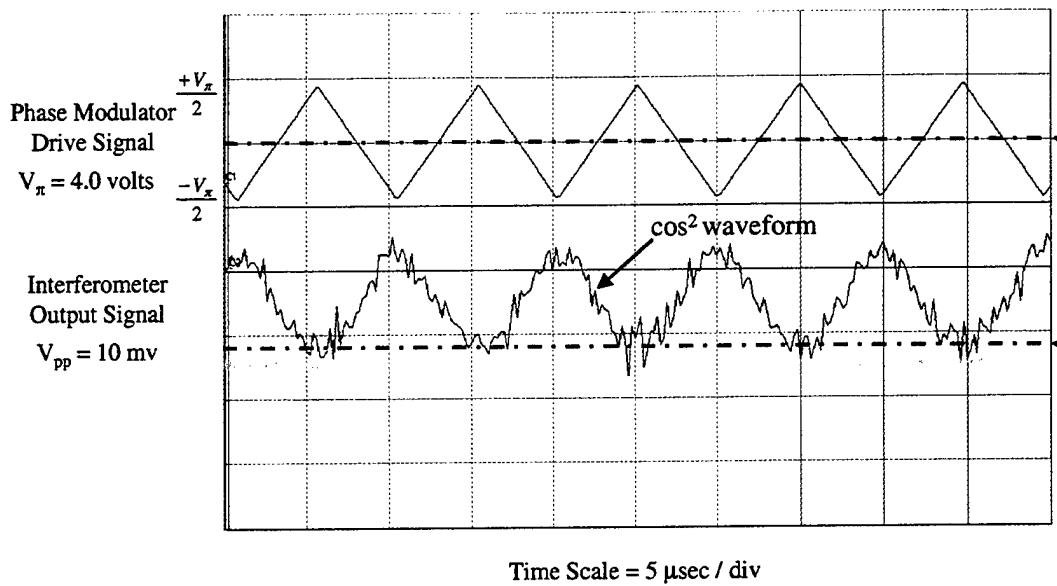


Figure 4.8 Results of the Phase Modulator Characterization Test.

E. SEMICONDUCTOR OPTICAL AMPLIFIER CHARACTERIZATION

The semiconductor optical amplifier (SOA) is a semiconductor laser device that can amplify an externally input optical signal. Unlike semiconductor lasers, semiconductor optical amplifiers are biased just below oscillation, but have enough gain to amplify light that passes through them. In SOAs, a drive current produces a population inversion by transferring electrons from the valence to the conduction band. In the presence of an optical field, the stimulated emission of these charge carriers produces a signal gain. [17].

The semiconductor optical amplifier for the fiber lattice accumulator is a JDS Uniphase CQF871, multi-quantum well, booster amplifier designed to provide gain to 1550-nm light sources. The maximum fiber-to-fiber gain is specified as 21.2 dB with a

saturation power output of 12 dBm. The SOA is designed to minimize optical reflections while maintaining low-noise operation [20].

In order to characterize the SOA, the device must be connected to a butterfly service mount, a temperature controller and a laser driver. The characterization test configuration is shown in Figure 4.9.

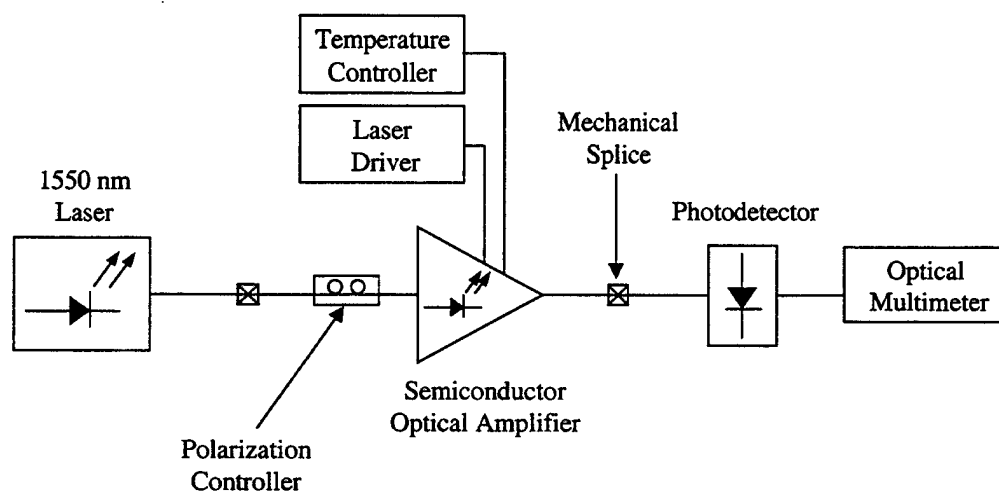


Figure 4.9 Block Diagram of the SOA Characterization Test.

The 1550-nm laser source was connected directly to the input of the SOA by a mechanical splice. The SOA was placed into the butterfly service mount specifically configured for the SOA pin configuration. A temperature controller and laser current driver were connected to the mount to properly control the SOA amplification. The output of the SOA was connected to an optical multimeter to determine the power output of the device. The results of this characterization test are displayed in Figure 4.10.

At low drive current, the device experienced very little power gain, but reached 0 dB gain at 26 mA. The gain of the device quickly increased as the drive current

increased, but provided marginal gain increases above 200 mA. The gain of the device saturated around 300 mA providing a total gain of 22.5 dB to the incoming light.

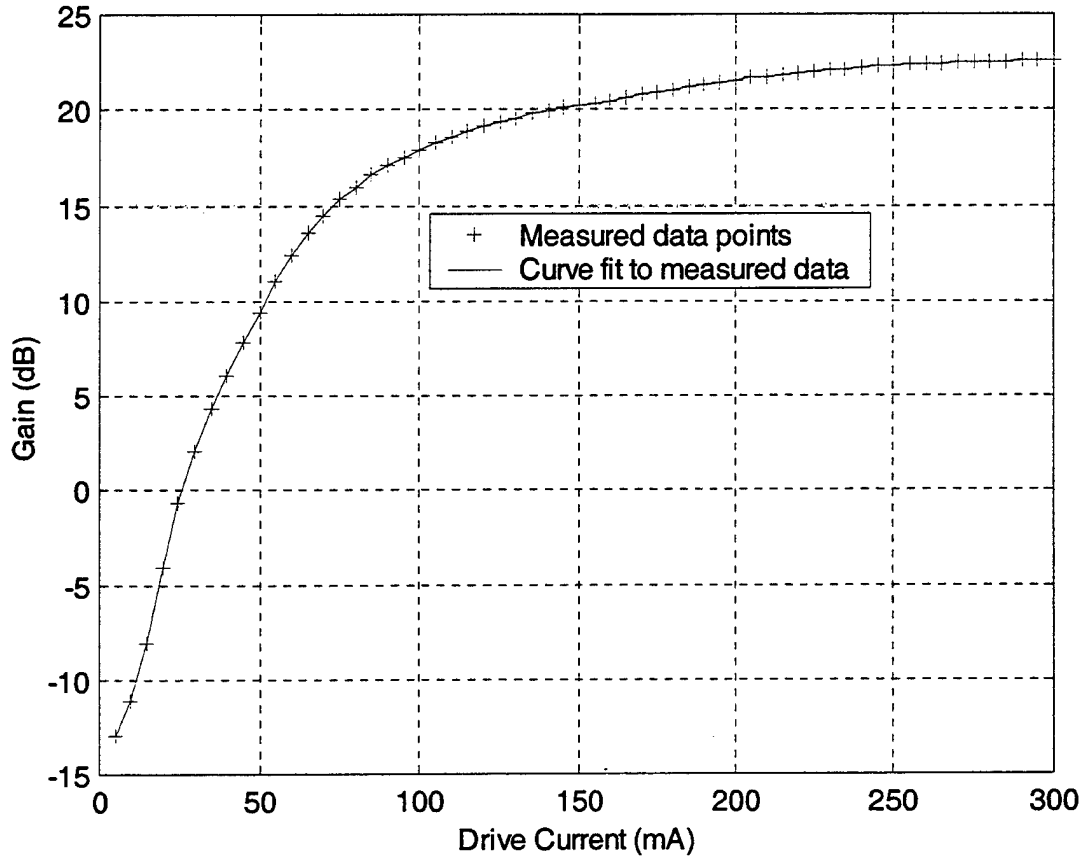


Figure 4.10 Results of the SOA Characterization Test.

In Figure 4.11, the range of acceptable gains required by the fiber lattice structure for selected variable ratio coefficients are plotted against the measured results of the characterization test. The gains required for a monotonic response of the fiber lattice range between 4.5 dB and 8.3 dB which correspond to a range for the drive current of 35 mA to 47 mA.

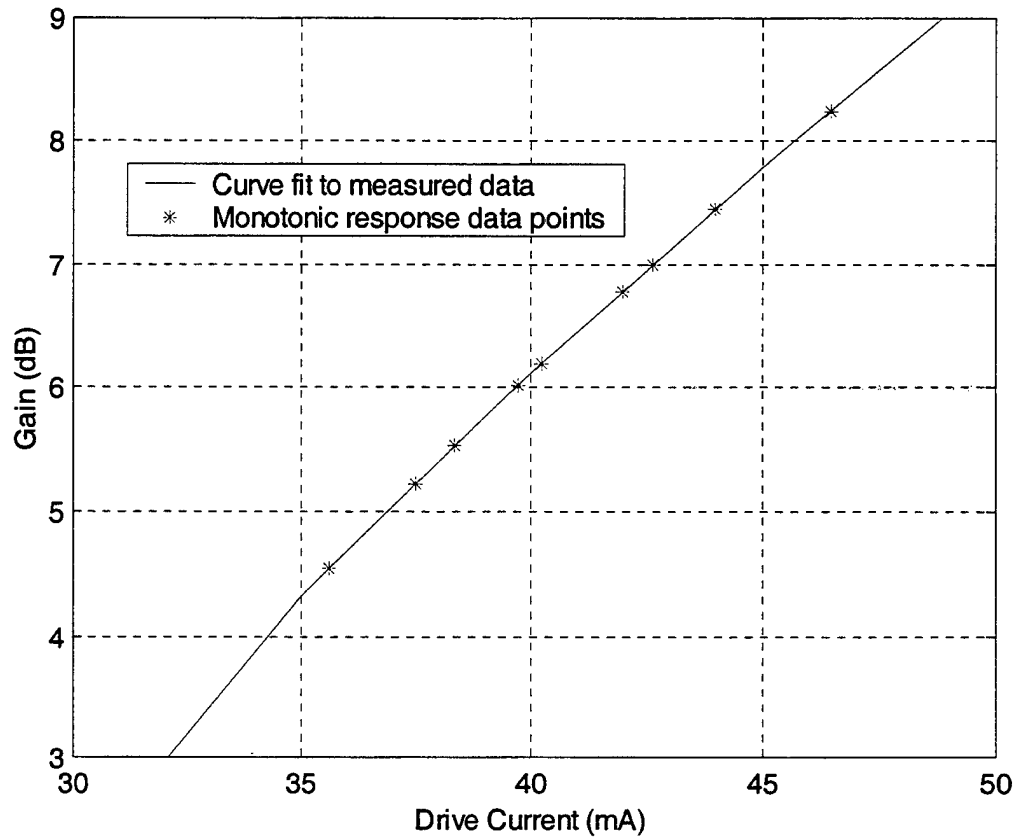


Figure 4.11 Various SOA Operating Points Required for Monotonic Response of the Fiber Lattice Accumulator

F. FIBER LATTICE ACCUMULATOR MEASUREMENTS

Once the phase modulator and the SOA were characterized, the fiber lattice accumulator was constructed and tested. In order to properly characterize the fiber lattice, the sampling and RF inputs were modified, the signal sampling subsystem initialized, and the coupling ratios of the directional couplers were matched to the gain of the SOA. Two waveform measurements were taken and their locations are labeled in Figure 4.13. The first measurement was at the output of the phase modulator (Y_1) and the second at the output of the fiber lattice accumulator (Y_2).

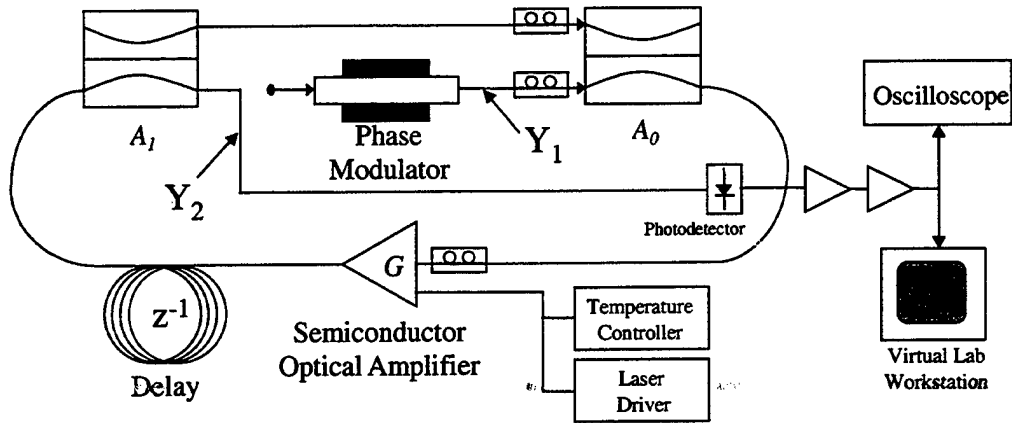


Figure 4.12 Fiber Lattice Accumulator Waveform Measurement Locations.

As described in Chapter III, the sampling laser system was driven with a 200-kHz analog square wave and an 8-kHz triangular wave was chosen for the RF antenna signal. While the signal frequencies were increased to match the 1/PRF delay in the fiber lattice, the oversampling ratio of 12.5 remained the same as in previous experiments. No changes were made to the signal sampling system. The magnitude MZI remained biased by +2.9 volts to provide the proper transmissivity characteristic with respect to the direction MZI. The output of the direction comparator circuit was set to provide 0 volts to the phase modulator for accumulation up and +4.0 volts for accumulation down.

In order to achieve a linear response from the fiber lattice accumulator, the coupling ratios of the variable ratio directional couplers must be matched to the gain of the SOA [7]. The coupling ratios are related to the SOA gain by the transfer function of the fiber lattice accumulator,

$$H_{12}(z) = \frac{(1 - a_0)(1 - a_1)Gz^{-1}}{1 - a_0a_1Gz^{-1}}. \quad 4.5$$

The coupling coefficients, or coupling ratios, of the directional couplers A_0 and A_1 are represented by a_0 and a_1 , respectively [5]. The gain of the SOA is represented by G . If $a_0a_1G < 1$, the output of the fiber lattice will saturate. Conversely, if $a_0a_1G > 1$, the output of the fiber lattice will grow exponentially. Therefore, the choice of the coupling coefficients and the SOA gain must be $a_0a_1G \approx 1$ to provide a linear response.

For this experiment, the variable ratio directional couplers were set to their 3-dB ratios, thus the coupling coefficients a_0 and a_1 were both equal to 0.5. The gain of the semiconductor, G , was set at 6 dB. From the results of the SOA characterization test, the 6 dB gain point equated to a drive current of 39.7 mA.

Since the output of the phase modulator, Y_1 , is the input to the fiber lattice, it was the first waveform measured. This waveform is displayed in Figure 4.13 (a). The output of the phase modulator qualitatively resembles the output of the magnitude MZI. This is expected since the phase modulator affects the phase of the light and does not affect the total light energy, or number of photons, received by the photodetector. The peak-to-peak voltage of the waveform was 0.34 volts.

The second waveform measured was the output of the fiber lattice, Y_2 , and it is displayed in Figure 4.13 (b). This waveform also resembles the output of the magnitude MZI and has a peak-to-peak voltage of 0.66 volts. In order to determine if the variable ratio couplers were working properly, first the A_0 and then the A_1 coupling ratios were varied from 0.5 to 0. In both cases, the waveform amplitude was attenuated and eventually disappeared as the ratio approached zero. Next, the gain of the SOA was

increased and decreased to determine its effect on the output of the fiber lattice. As the gain was increased, the shape of the waveform remained unchanged yet the peak-to-peak voltage increased. Likewise, when the gain was decreased, the peak-to-peak voltage decreased.

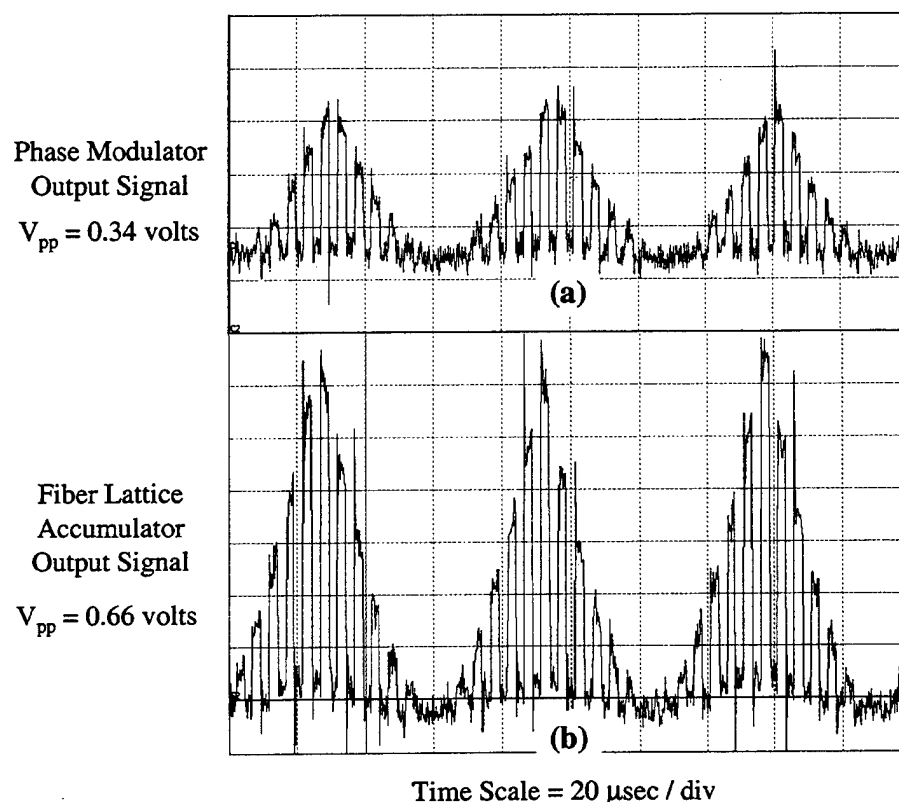


Figure 4.13 Comparison of (a) the Phase Modulator and (b) Fiber Lattice Accumulator Output Signals.

In order to better understand what was occurring within the fiber lattice accumulator, a MATLAB simulation was created. In the first run of the simulation, coherent accumulation was assumed at the A_0 coupler (i.e., when the RF input voltage increases, the fiber lattice accumulates up and when it decreases, the fiber lattice accumulates down). The results from this simulation are displayed in Figure 4.14 (a).

The second run of the simulation assumed incoherent accumulation within the fiber lattice. In this case, constructive and destructive interference at the A_0 coupler is not assumed, and only amplification of the signal results. The results of this simulation are displayed in Figure 4.14 (b).

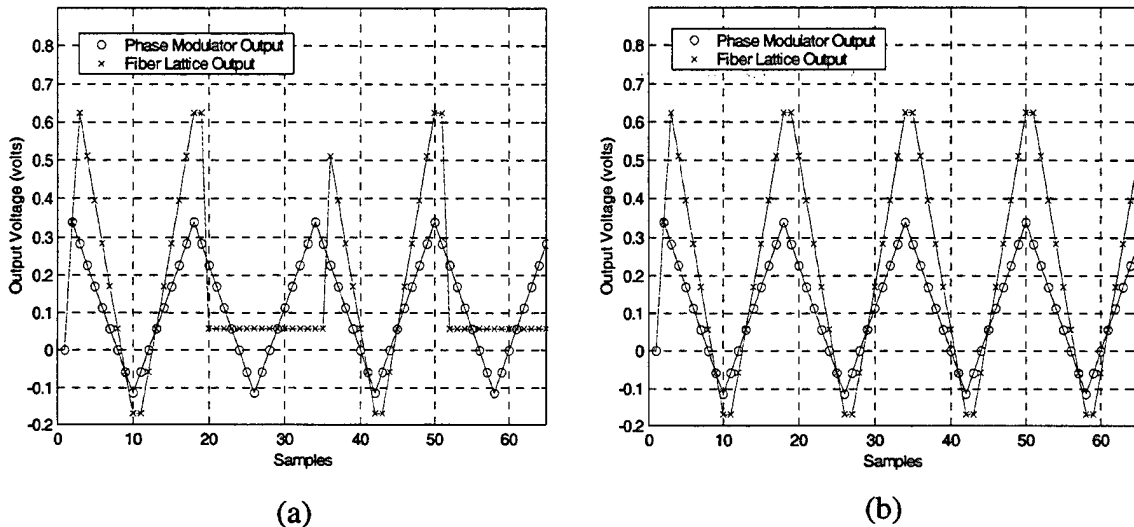


Figure 14.14 MATLAB Comparison of the Fiber Lattice Output versus the Phase Modulator Output for (a) Coherent Accumulation and (b) Incoherent Accumulation.

The results in Figure 4.14 (b) qualitatively and quantitatively match the results of the measured waveforms in Figure 4.13 (a) and (b). In the MATLAB simulation, the amplitudes of the samples from the fiber lattice output are twice the amplitudes of the phase modulator output samples. This same effect is displayed in the measured samples in Figure 4.13.

One of the problems discovered with the fiber lattice accumulator was that the fiber delay loop had been included as part of the feedback path of the fiber lattice structure. The fiber delay loop was not in the feed-forward path as shown in Figure 4.12,

but instead was placed in the upper path (feedback path) from the A_I directional coupler to the A_0 directional coupler. This, however, resulted in a transfer function different from the expected transfer function in Equation 4.5. The resulting transfer function is,

$$H_{FB}(z) = \frac{(1-a_0)(1-a_1)G}{1-a_0a_1Gz^{-1}}. \quad 4.6$$

This transfer function is a first-order, all-pole system and has one zero at the origin. Following the analysis in Reference 5, the pole at $z = 1$ (i.e., when $a_0a_1G = 1$) will be stable, but any increase in the gain of the SOA or the coupling coefficients will quickly result in instability of the $\Sigma\Delta$ modulator. Likewise a decrease in the SOA gain or in the coupling coefficients will result in settling and saturation of the $\Sigma\Delta$ modulator. Therefore, this particular design of the fiber lattice is not desired, and the fiber delay loop was removed and placed in the feed-forward loop.

With the fiber delay loop moved to the feed-forward loop as shown in Figure 4.12, the experiment was conducted again. The variable ratio directional couplers were set to their 3-dB ratios, and the gain of the semiconductor, G , was set at 6 dB. The waveform output from the phase modulator, Y_1 , was compared with the output waveform of the fiber lattice accumulator, Y_2 . The result of this experiment showed no change to the output of the fiber lattice accumulator from the results displayed in Figure 4.13 (b). This provided a good indication that the coherence required for constructive and destructive interference in the A_0 directional coupler was not being achieved.

In order to determine the source of the problem, the first component examined was the comparator circuit; however, it was verified to be working properly. The output of the comparator circuit matched the output shown in Figure 4.6. Other possible reasons for the incoherent operation could be a damaged phase modulator or a timing problem between the comparator circuit and the arrival of light pulses from the magnitude MZI. If the voltage arrives anytime before or after the pulses, the desired phase delay will not be achieved. However, the most likely cause of the incoherent accumulation is the wide spectral width of the 1550-nm Fabry-Perot laser. Due to its design, the Fabry-Perot laser emits several longitudinal modes at once, spreading its output power over a range of wavelengths. For coherent accumulation, a monochromatic, or single wavelength, laser such as a distributed feedback (DFB) laser is required. A 1550-nm DFB laser (Lucent Technologies, Model A1112) with a linewidth of less than 3 MHz has been identified as a possible replacement for the Fabry-Perot laser.

G. SUMMARY

In this chapter, the results of the testing and evaluation of the electro-optical $\Sigma\Delta$ modulator have been presented. The optical losses in both the signal oversampling subsystem and the electro-optical $\Sigma\Delta$ system were characterized and closely matched the calculated optical losses. The operation of the signal oversampling system was analyzed and showed proper amplitude-modulating of the 2-kHz RF antenna signal. The transfer functions for the magnitude and direction MZIs were compared to the theoretical transfer functions. The transfer functions qualitatively matched those obtained by computer simulation. Proper operation of the direction comparator circuit was also demonstrated.

Finally, operation of the fiber lattice accumulator was evaluated. Coherent accumulation was not observed, but the output signal did demonstrate the expected amplification.

THIS PAGE INTENTIONALLY LEFT BLANK

V. CONCLUSIONS AND RECOMMENDATIONS

A. LIMITATIONS

While the NPS first-order, single-bit, electro-optical sigma-delta ($\Sigma\Delta$) modulator is designed for sampling microwave frequency signals, this thesis focused on construction of a low frequency prototype. The approach was to first determine the operating characteristics of the $\Sigma\Delta$ modulator before optimizing it for high frequency operations. This approach was well suited for laboratory applications since some components and test equipment used in the construction of the NPS $\Sigma\Delta$ modulator are bandwidth limited. For example, the Wavetek function generator used to drive the laser lacks the high frequency components required for sampling frequencies beyond 14 MHz. Within the $\Sigma\Delta$ modulator itself, the limiting electro-optical component is the phase modulator with an upper bandwidth of 500 MHz.

The primary limitation to the operation of the electro-optical $\Sigma\Delta$ modulator is not the bandwidth of the electro-optical components, but rather the length of the fiber lattice accumulator. Since the delay in the fiber lattice is inversely proportional to the PRF of the sampling laser, a shorter fiber lattice allows a faster sampling frequency. If the fiber lattice components are assumed to have 5.5 cm pigtails for fusion splicing operations, the total length would be 0.52 meters. This equates to an upper sampling frequency of 392 MHz, below the bandwidth limitation of the phase modulator. Therefore, to achieve higher frequency sampling rates, the fiber lattice delay becomes the limiting factor. Any

future testing of the $\Sigma\Delta$ modulator will have to consider the physical length of the fiber lattice accumulator.

The other limitation of the electro-optical $\Sigma\Delta$ modulator is the fixed length of the fiber lattice accumulator. Fixing the length of the fiber lattice in effect establishes the sampling frequency of the drive laser. While this may not pose a problem for application-specific electro-optical $\Sigma\Delta$ modulators, it does restrict the flexibility of the engineer to vary the sampling frequency for testing purposes. Therefore, care must be taken to first select the sampling frequency before constructing the fiber lattice accumulator.

The final potential limitation of the $\Sigma\Delta$ modulator is the use of the Fabry-Perot laser as the signal sampling system. A Fabry-Perot laser, due to its design, has an inherently wide spectral width. This spectral line width distributes the power of the laser sampling pulses across a range of wavelengths. Therefore, a multiple of wavelengths exist in each pulse precluding coherent accumulation within the fiber lattice.

B. CONCLUSIONS

Using computer simulations of the electro-optical $\Sigma\Delta$ modulator as a model, a physical prototype was constructed and evaluated. For demonstration purposes, the electro-optical $\Sigma\Delta$ modulator was constructed to sample a 2 kHz signal by an oversampling ratio (OSR) of 12.5. However, the system can be modified to oversample a 3 MHz signal with an OSR of 128, by reducing the length of the fiber lattice accumulator.

The signal oversampling system in this thesis utilized a pulse modulated 1550-nm laser source to provide oversampling of an RF antenna signal. The RF signal was successfully amplitude-modulated by two Mach-Zehnder interferometers and coupled into the optical domain. The magnitude MZI transfer function was biased $+V_{\pi}/2$ volts with respect to the direction MZI. The results confirmed the transmissivity functions of the magnitude and direction MZIs required for coherent sampling of the RF antenna waveform.

A simple comparator circuit was constructed and tested in conjunction with the signal oversampling subsystem. The comparator circuit demonstrated proper operation in the presence of the input signal from the direction MZI. When the input signal was below the threshold, a 4.0 volt DC signal was delivered. When the input signal exceeded the comparator threshold, the signal output was 0 volts. However, during the period when the samples from the direction MZI were above the comparator threshold, a cycle of 2.2 volts was observed from the comparator circuit. It was determined that this was caused by the output of the photodetector cycling across the comparator threshold in response to the presence/absence of the optical signal.

A thorough analysis was performed on the optical losses in both the signal oversampling system and the electro-optical $\Sigma\Delta$ system as a whole. The results of the measured power losses were consistent with the calculated losses in the system. Additionally, it was shown that the system has sufficient power margin to withstand additional losses.

Finally, the fiber lattice accumulator was constructed and tested. The results of the output from the fiber lattice differed from the expected results. One possible explanation is that the phase relationships required for accumulation up and accumulation down are not being met by the phase modulator and direction comparator circuit. Another possibility is the multi-mode operation of the Fabry-Perot laser system used in the testing of the fiber lattice accumulator.

C. RECOMMENDATIONS

Characterizing the operation of the fiber lattice is critical to determining the performance of the electro-optical $\Sigma\Delta$ modulator. Further analysis is necessary to determine the proper matching of the coupling coefficients of the variable ratio couplers to the gain of the semiconductor optical amplifier. A full systems approach should be taken to analyze the fiber lattice accumulator, to include evaluating the signal response at each component within the fiber lattice.

A more detailed analysis of the current operation of the fiber lattice accumulator will aid in the design of the fiber lattice output comparator circuit. This comparator circuit can be modeled after the direction path comparator circuit. The comparator will deliver the feedback voltage to the Mach-Zehnder interferometers to complete the push-pull configuration required for $\Sigma\Delta$ modulation. At this point, a complete analysis of the electro-optical $\Sigma\Delta$ modulator can be done to include an analysis of the leaky modes.

Finally, the 1550-nm Fabry-Perot laser should be replaced with a narrow linewidth, distributed feedback (DFB) laser. The single-mode operation of the DFB

would minimize the chromatic dispersion in the $\Sigma\Delta$ modulator and enable coherent accumulation within the fiber lattice.

THIS PAGE INTENTIONALLY LEFT BLANK

APPENDIX A. COMPONENTS AND EQUIPMENT

A. OPTICAL COMPONENTS

- 1550 nm Fabry-Perot Laser
Broadband Communications Products
Model 400A
Replace with 1550 nm DFB laser
- 2 x 2, 50/50 3 dB Coupler
Newport Corporation
Part No. F-CPL-F22155
- PolaRite™ Polarization Controller
Newport Corporation
Part No. F-POL-IL
Quantity: 3
- Fiber Polarization Controller
ThorLabs, Inc.
Part No. FPC010
Quantity: 3
- Mach-Zehnder Interferometer; 1550 nm, 3 GHz
JPS Uniphase – Uniphase Telecommunications Products
Part No. MZ150-000560
Quantity: 2
- Phase Modulator, 1550 nm, 0.5 GHz
JPS Uniphase – Uniphase Telecommunications Products
Part No. PM150-000171
- High-Speed Photodetector, 12 ps IR
New Focus, Inc.
Model 1024
Quantity: 2
- Variable Ratio Coupler
Newport Corporation
Part No. F-CPL-V
Quantity: 2

- Semiconductor Optical Amplifier
JDS Uniphase – Uniphase Netherlands B.V.
Part No. CQF871/0

B. ELECTRICAL EQUIPMENT

- Pulse Function Generator, 20 MHz
Wavetek Wandel Goltermann, Inc.
Model 145-S-872
Quantity: 2
- RF Amplifier, 1 kHz – 150 MHz
Hewlett-Packard Company
Model 461A
Quantity: 4
- Dual Power Supply
Tektronix
Model PS503A
- DC Power Supply
Global Specialties
Model 1300
Quantity: 2
- High Speed Dual Comparator Chip
National Semiconductor Corporation
Model LM319
- Butterfly PIN Laser Diode Mount
ILX Lightwave Corporation
Model LDM-4984
- Temperature Controller
ILX Lightwave Corporation
Model LDT-5412
- Laser Diode Driver
Spectra Diode Labs
Model SDL-800

C. TEST AND OTHER EQUIPMENT

- Oscilloscope, 200 MHz
Tektronix Corporation
Model 2445B
- VirtualBench Software
National Instruments Corporation
Version 2.1.1
- Optical Multimeter
ILX Lightwave Corporation
Model OMM-6810
- Optical Fiber Fusion Splicing Machine
Sumitomo Corporation - Sumitomo 11X
Sumitomo Corporation - Type 36
Sumitomo Corporation - Type 35SE-RC

THIS PAGE INTENTIONALLY LEFT BLANK

APPENDIX B. CONNECTIONS AND CONFIGURATION OF THE INTEGRATED, OPTICAL SIGMMA-DELTA MODULATOR

There are two main systems in the configuration of the $\Sigma\Delta$ modulator: the signal oversampling subsystem and the fiber lattice accumulator. Figure B.1 shows the complete layout of the $\Sigma\Delta$ modulator.

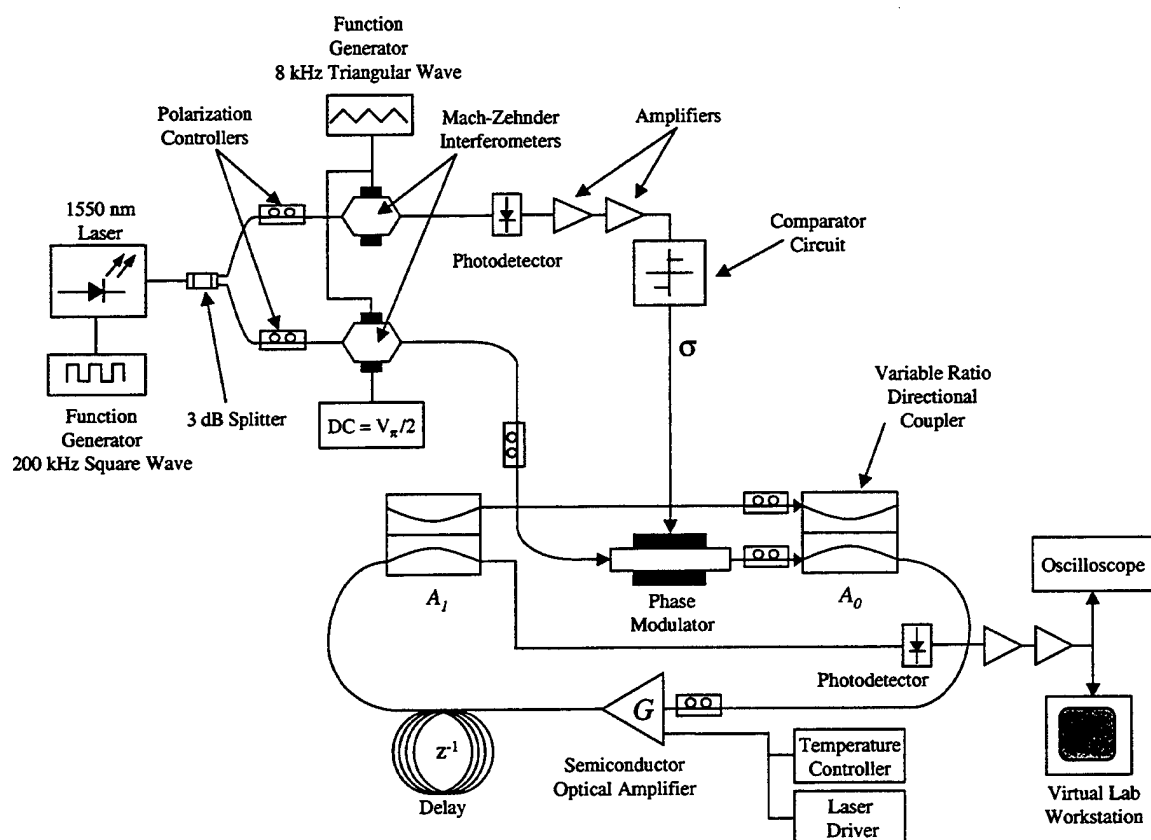


Figure B.1 Layout and Connections for the NPS Electro-Optical $\Sigma\Delta$ Modulator.

THIS PAGE INTENTIONALLY LEFT BLANK

APPENDIX C. MATLAB PROGRAMS

This appendix shows some of the MATLAB programs created to support the discussion in the test.

```
% Urban Gillespie
% 4 November 2000
% Semiconductor Optical Amplifier Characterization (Gain vs Drive
Current)

% Measured optical power and drive current values
Pin = 0.0676; % Milliwatts
D_current = 0:5:300; % Milliamps
Pout = [0, 0.00345, 0.00525, 0.01047, 0.0262, 0.0582, 0.1088,
0.1831...0.2767, 0.4060, 0.5839, 0.8683, 1.19, 1.55, 1.91, 2.31,
2.67...3.07, 3.44, 3.79, 4.17, 4.52, 4.86, 5.20, 5.54, 5.86, 6.14,
6.44...6.71, 6.99, 7.18, 7.25, 7.49, 7.81, 8.09, 8.37, 8.60, 8.88,
9.12...9.36, 9.60, 9.85, 10.05, 10.26, 10.43, 10.64, 10.84, 11.01,
11.17...11.30, 11.43, 11.56, 11.66, 11.76, 11.84, 11.91, 11.97,
12.03...12.07, 12.11, 12.14]; % Milliwatts

% Calculate the optical gain
Gain_dB = 10.*(log10(Pout./Pin));

% Amplifier gains for monotonic response of the fiber lattice
M_Gain = [2.85, 3.333, 3.57, 4.0, 4.166, 4.76, 5.0, 5.55, 6.67];
M_Gain_dB = 10.*log10(M_Gain);
M_current = interp1(Gain_dB, D_current, M_Gain_dB, 'linear');

% Plot the measured results from the SOA testing
figure(1);
plot(D_current, Gain_dB, 'r+', D_current, Gain_dB, 'b-');

%title('Semiconductor Optical Amplifier Gain vs Drive Current');
xlabel('Drive Current (mA)'); ylabel('Gain (dB)');
legend('measured data points', 'curve fit of measured data', 2);
grid on;

% Plot gains and drive currents required for a monotonic fiber
% lattice response
figure(2);
plot(D_current, Gain_dB, 'b-');
axis([30,50,3,9]);
hold on;
plot(M_current, M_Gain_dB, 'r*');
```

```

%title('Required Drive Current for Monotonic Fiber Lattice
Gain');
xlabel('Drive Current (mA)'); ylabel('Gain (dB)');
legend('curve fit of measured data', 'monotonic response
data points', 2);
grid on;

```

Program C1: MATLAB program is used to plot the gain performance of the semiconductor optical amplifier as a function of the drive current.

```

% Urban Gillespie
% 30 November 2000
% Calculate the system optical loss
% Results for Chapter 4, Section A2.

% Initialize Data
Pin = -3.135;% Power into the system from the pulsed laser (dBm)
LtoA0 = -10.318; % The dB loss up to the A0 directional coupler (dB)
LfmA0toA1 = 2.911; % The dB gain in the feed-forward loop to A1
LfmFLout = 3.33; % The db loss in the fiber lattice output arm
LfmFB = 3.22; % Sum of losses from A1 & the feedback loop (dB)
PtoA0 = 10^(LtoA0/10); % The expected power at the A0 directional
coupler (mW)
PfmA1 = 0; % Initialize the power in the feedback loop (mW)
N = 11; % Number of iterations

% Recursively calculate the output power of the fiber lattice
for i=1:N
PoutA0 = PfmA1 + PtoA0;% Add power from the PM & the feedback loop (mW)
PoutA0 = 10*log10(PoutA0/2);% Convert to dBm
PinA1 = PoutA0 + LfmA0toA1;% Power into the A1 directional coupler (dBm)

Pout = PinA1 - LfmFLout;% Calculate the power out of the lattice (dBm)
Pout = 10^(Pout/10); % Convert to mW
PfmA1 = PinA1 - LfmFB;% Calculate the power in the feedback loop (dBm)
PfmA1 = 10^(PfmA1/10);% Convert the power in the feedback loop to mW
end

Pout %Power out of the fiber lattice

```

Program C2: MATLAB program used to calculate the electro-optical $\Sigma\Delta$ modulator optical loss.

```

% Urban Gillespie
% 3 December 2000
% Comparison of coherent & incoherent fiber lattice accumulation
% Results for Chapter 4, Section F.

% Sampled version of the output of the phase modulator
Vin = [0 12 10 8 6 4 2 0 -2 -4 -2 0 2 4 6 8 10 12 10 8 6 4 2 0 -2 -4 ...
      -2 0 2 4 6 8 10 12 10 8 6 4 2 0 -2 -4 -2 0 2 4 6 8 10 12 10 8 ...
      6 4 2 0 -2 -4 -2 0 2 4 6 8 10 12];

% Scale the output of the phase modulator
factor = 0.34/12;
Vin = factor.*Vin;

% Set the coupling coefficients and the SOA gain
a0 = 0.5;
a1 = 0.5;
gain = 4;

% Apply normal accumulation within the fiber lattice
for i = 1:(length(Vin)-1)
    if i<19
        Vout(i) = (4*((Vin(i+1) + Vin(i))/2))/2;
    end
    if i>18 & i<35
        Vout(i) = (4*((abs(Vin(i+1) - Vin(i)))/2))/2;
    end
    if i>34 & i<51
        Vout(i) = (4*((Vin(i+1) + Vin(i))/2))/2;
    end
    if i>50
        Vout(i) = (4*((abs(Vin(i+1) - Vin(i)))/2))/2;
    end
end

% Create the x-axis of sampled values
xaxis1 = 1:length(Vin);
xaxis2 = 2:(length(Vin));

% Output the results
figure(1)
plot(xaxis1, Vin, 'bo', xaxis2, Vout, 'rx')
hold on;
plot(xaxis1, Vin, 'b-', xaxis2, Vout, 'r-');
xlabel('Samples'); ylabel('Output Voltage (volts)');
legend('Phase Modulator Output','Fiber Lattice Output', 2);
grid on;
axis([0,65,-0.2,0.9]);

% Apply "constructive only" accumulation within the fiber lattice
for i = 1:(length(Vin)-1)
    Vout(i) = (gain*((Vin(i+1) + Vin(i))*a0))*a1;
end

% Output the results
figure(2)
plot(xaxis1, Vin, 'bo', xaxis2, Vout, 'rx')
hold on;

```

```
plot(xaxis1, Vin, 'b-', xaxis2, Vout, 'r-');  
xlabel('Samples'); ylabel('Output Voltage (volts)');  
legend('Phase Modulator Output', 'Fiber Lattice Output', 2);  
grid on;  
axis([0,65,-0.2,0.9]);
```

Program C3: MATLAB program used to plot the expected output of the fiber lattice for coherent and incoherent accumulation.

LIST OF REFERENCES

1. Norsworthy, S.R., Schreier, R. and Temes, G.C., *Delta-Sigma Data Converters – Theory Design and Simulation*, IEEE Press, 1997.
2. Pace, P.E., Ying, S.T., Powers, J.P., and Pieper, R.J., “Integrated Optical Sigma-Delta Modulators,” *Optical Engineering*, Vol. 35, pp. 1828-1836, July 1996.
3. Ying, S.J., “Integrated Optical Sigma-Delta Modulators,” Master’s Thesis, Naval Postgraduate School, Monterey, CA, September 1995.
4. Bewley, S.A., “Fiber Lattice Accumulator Design Considerations for Optical $\Sigma\Delta$ Digital Antennas,” Master’s Thesis, Naval Postgraduate School, Monterey, CA, December 1998.
5. Atherton, A.F., “Integrated Optical Fiber Lattice Accumulators,” Master’s Thesis, Naval Postgraduate School, Monterey, CA, March 1997.
6. DeCusatis, C., *et al.*, *Handbook of Fiber Optic Data Communication*, Academic Press, Chestnut Hill, MA, 1998.
7. Pace, P., Bewley, S., and Powers, P., “Fiber-Lattice Accumulator Design Considerations for Optical Sigma-Delta Analog-to-Digital Converters,” *Optical Engineering*, Vol. 39, pp. 1517-1526, June 2000.
8. Aziz, P.M., Sorensen, H.V., and Van der Spiegel, J., “An Overview of Sigma-Delta Converters,” *IEEE Signal Processing*, Vol. 13, pp. 61-84, January 1996.
9. Candy, J.C. and Temes, G.C., “Oversampling Methods for A/D and D/A Conversion,” *Oversampling Delta-Sigma Data Converters*, J.C. Candy and G.C. Temes, Eds., pp. 1-29, IEEE Press, New York, NY, 1992.
10. Pace, P.E., *Advanced Techniques for Digital Receivers*, Artech House, Inc., Norwood, MA, June 2000.
11. Stewart, R.W., “An Overview of Sigma-Delta ADCs and DAC Devices,” IEE Colloquium on Oversampling and Sigma-Delta Strategies for DSP, Vol. 1, pp. 1-9, 1995.
12. Powers, J. P., *An Introduction to Fiber Optic Systems*, Second Edition, Richard D. Irwin, Chicago, IL, 1997.
13. Hecht, J., *Understanding Fiber Optics*, Howard W. Sams & Company, Indianapolis, IN, 1987.

14. Optics for Research, *Fiber-Optic Products*, Product Catalogue, Caldwell, NJ 1997.
15. Hentschel, C., *Hewlett Packard Fiber Optics Handbook*, Second Edition, Hewlett Packard Company, Palo Alto, CA, 1988.
16. Broadband Communications Products, Inc., *BCP Model 400A Laser Transmitter User's Manual*, Rev B, 7 April 1997.
17. Kazovsky, L., Benedetto, and S., Willner, A., *Optical Fiber Communication Systems*, Artech House, Inc., Norwood, MA, 1996.
18. JDS Uniphase, JDS Uniphase MZ150-000560 Final Test Data Sheet, 19 October 1999.
19. JDS Uniphase, JDS Uniphase PM150-000171 Final Test Data Sheet, 12 October 1999.
20. JDS Uniphase, *JDS Uniphase CQF871/0 1550 nm MQW Semiconductor Optical Booster Amplifier Specification Sheet*, January 1999.

INITIAL DISTRIBUTION LIST

	No. of Copies
1. Defense Technical Information Center2 8725 John J. Kingman Rd., STE 0944 Ft. Belvoir, VA 22060-6218	
2. Dudley Knox Library2 Naval Postgraduate School 411 Dyer Rd. Monterey, CA 93943-5101	
3. Chairman, Code EC.....1 Department of Electrical and Computer Engineering Naval Postgraduate School Monterey, CA 93943-5121	
4. Prof. Phillip E. Pace, Code EC/Pc.....2 Department of Electrical and Computer Engineering Naval Postgraduate School Monterey, CA 93943-5121	
5. Prof. John P. Powers, Code EC/Po 2 Department of Electrical and Computer Engineering Naval Postgraduate School Monterey, CA 93943-5121	
6. Dr. David Honey (RFLICS).....1 DARPA / Microsystems Technology Office 3701 North Fairfax Drive Arlington, VA 22203-1714	
7. Dr. James Murphy (PACT).....1 DARPA / Microsystems Technology Office 3701 North Fairfax Drive Arlington, VA 22203-1714	
8. Dr. Robert Leheny (Ultra Photonics).....1 DARPA / Microsystems Technology Office 3701 North Fairfax Drive Arlington, VA 22203-1714	

9. Dr. Richard Williamson.....1
MIT Lincoln Laboratory
244 Wood Street
Room LL-C-317
Lexington, MA 02420-9108
10. Prof. Ronald J. Pieper, Code EC/Pi..... 1
Department of Electrical and Computer Engineering
Naval Postgraduate School
Monterey, CA 93943-5121
11. Urban Gillespie.....1
4601 Silver Oak Street
Dayton, OH 45424